RESEARCH ARTICLE

Key Points:
- Haladala gabbros hosting V-Ti magnetite deposits are the earliest magmatism of Tarim mantle plume
- Haladala layered gabbros record the process of the plume-orogenic lithosphere interaction
- The Southwest Tianshan Orogen was impacted by an upwelling mantle plume at ~ 300 Ma

Plume-orogenic lithosphere interaction recorded in the Haladala layered intrusion in the Southwest Tianshan Orogen, NW China

**Peng-Li He[1,2], Xiao-Long Huang[1], Yi-Gang Xu[1], Hong-Yan Li[1], Xue Wang[1,2], and Wu-Xian Li[1]**

[1]State Key Laboratory of Isotope Geochemistry, Guangzhou Institute of Geochemistry, Chinese Academy of Sciences, Guangzhou, China, [2]University of Chinese Academy of Sciences, Beijing, China

Abstract The plume-orogenic lithosphere interaction may be common and important for the generation of large igneous provinces. The information regarding such a process is recorded by the Haladala gabbroic intrusion (~300 Ma), the largest layered ultramafic-mafic intrusion hosting V-Ti magnetite deposits in the Southwest Tianshan Orogen, NW China. The Haladala gabbros exhibit unfractionated chondrite-normalized rare earth element patterns with negative Nb and Ta anomalies and positive Pb anomaly on the primitive mantle-normalized multielement variation diagram. They are characterized by low initial Sr isotopes, slightly decoupled but high positive bulk rock $\varepsilon_{Nd}(t)$ and $\varepsilon_{Hf}(t)$, and high $^{207}Pb/^{204}Pb$ and $^{208}Pb/^{204}Pb$ relative to $^{206}Pb/^{204}Pb$, delineating a DUPAL signature in the sources. The Haladala gabbros cannot be arc or postcollisional magmatism, given the lack of hydrous minerals and low K contents, respectively. This is further supported by the relatively low oxygen fugacity required for the gradual enrichment of V-Ti magnetite during the magma fractionation and by an overall anhydrous mantle source suggested by troctolite mineral assemblage (olivine + plagioclase). The emplacement age of the Haladala gabbros is identical to that of the Wajilitag kimberlites in the Tarim's interior, which have been interpreted as the first magmatic expression of the Tarim mantle plume. We thus propose that the Haladala gabbroic intrusion was generated in a hybrid geodynamic setting in which the Southwest Tianshan Orogen was impacted by an upwelling mantle plume. In this sense, the Haladala layered gabbroic intrusion records the early phase of magmatism of the Tarim plume, which was preferentially emplaced in a lithospheric weak zone.

1. Introduction

Plume-lithosphere interactions are widely considered important in the generation of large igneous provinces (LIPs). Intensive investigation has been carried out on the passive and active role of the lithosphere in relation to flood volcanism, and on the quantitative contributions of plume, lithospheric mantle, and crust to flood volcanism [e.g., *Ellam et al.*, 1992; *Gallagher and Hawkesworth*, 1992; *Gibson et al.*, 1995; *Pik et al.*, 1999; *Li et al.*, 2012a; *Rocha et al.*, 2012; *Wei et al.*, 2014]. Orogenic lithosphere may also suffer pervasive modification by hot spot processes [*Villemaire et al.*, 2012] such as plume materials ascent to surface or ponding at the base of the lithosphere [e.g., *Sleep et al.*, 2002], or the heating and partial melting of the lower crust and lithospheric mantle, leading to delamination [e.g., *Saleeby et al.*, 2003]. On the other hand, the postcollisional extension tectonics of an orogenic belt may provide access for plume materials, lithospheric mantle-derived mafic-ultramafic rocks [*Murphy et al.*, 1998], and lower crust-derived felsic rocks [*Betts et al.*, 2009]. Therefore, plume-orogenic lithosphere interaction may be common and important for the generation of LIPs. However, little is known regarding magma generation processes associated with mantle plume upwelling beneath an orogenic belt, or how the orogen architecture might control the emplacement and composition of plume-derived magmas.

The Haladala gabbroic intrusion is one of the largest layered ultramafic-mafic intrusions in the Southwest Tianshan Orogen, NW China (Figure 1), and has the potential of economic V-Ti magnetite deposits based on outcrops of magnetite-rich layers [*Gao et al.*, 1991; *Lin and Deng*, 1996; *Long et al.*, 2012]. Layered mafic-ultramafic complexes occur in various tectonic settings, such as island arc (Alaskan type) [e.g., *Beard*, 1986], ophiolites [e.g., *Christensen and Smewing*, 1981], intracontinental rift system [e.g., *Bowles et al.*, 2013], or mantle plume [e.g., *Zhou et al.*, 2005; *Cawthorn and Ashwal*, 2009]. Nevertheless, V-Ti magnetite-bearing layered mafic-ultramafic complexes are largely restricted in the intraplate igneous
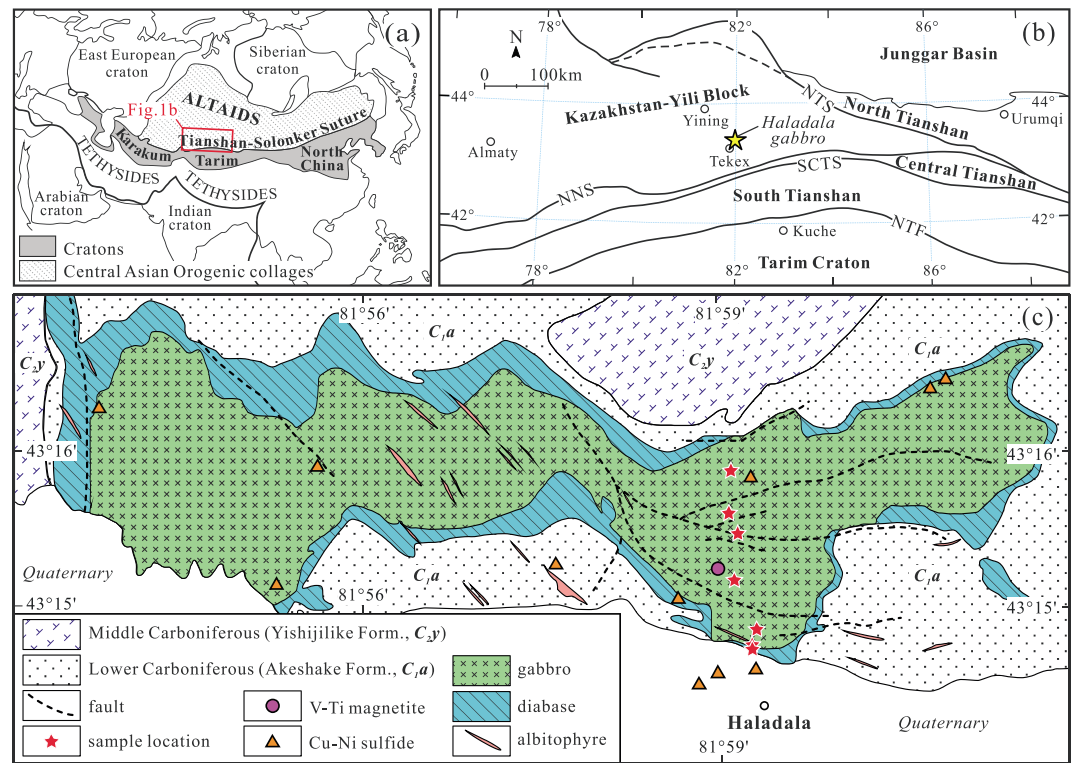
Figure 1. (a) Schematic map showing the position of the Tianshan orogenic collage and other collages in Asia, modified after *Şengör et al.* [1993]. (b) Tectonic sketch map of the western Tianshan orogenic belt, modified after *Qian et al.* [2009]. Abbreviations of fault and sutures: North Tianshan Suture (NTS), Nikolaev Line-North Nalati Suture (NNS), South Central Tianshan Suture (SCTS), North Tarim Fault (NTF). (c) Geological sketch map showing outcrop of the Haladala layered gabbroic intrusion, modified after *Gao et al.* [1991].

provinces related to mantle plumes [*Pirajno*, 2000], and to a lesser degree related to mantle upwelling through a slab window in a subduction setting, such as Beja Igneous complex, Southern Iberia Variscan Belt [*Pin et al.*, 2008]. Notable examples associated with mantle plumes include the Bushveld complex in South Africa [e.g., *Cawthorn and Ashwal*, 2009], Skaergaard Layered Series in Greenland [e.g., *Brooks et al.*, 1999], and Panzhihua complex in Southwest China [e.g., *Zhou et al.*, 2005]. He et al. [2013] and Long et al. [2012] proposed that the Haladala gabbroic intrusion was genetically related to the Tarim mantle plume. However, the Haladala intrusion was emplaced in the Tianshan orogenic belt, rather than within the plate's interior. Specifically, the Southwest Tianshan Orogen is located to the north of the Tarim Basin where Early Permian flood basalts were erupted [*Tian et al.*, 2010; *Yu et al.*, 2011; *Xu et al.*, 2014]. If the intrusion is plume related, then a better understanding of its genesis will yield new knowledge as to the nature of plume-orogenic lithosphere interaction.

It has been widely accepted that LIP is related to mantle plume originating from a thermal boundary at the core-mantle boundary [e.g., *Morgan*, 1971; *Campbell*, 2007; *Campbell and Griffiths*, 1990] or from the upper mantle/lower mantle transition zone [*Courtillot et al.*, 2003; *White and McKenzie*, 1989]. However, the issue on the formation of LIPs remains controversial. Some typical flood basalt provinces were even considered to be genetically related to the subduction processes, such as the Columbia River flood basalts [*Stefano et al.*, 2011; *Cabato et al.*, 2015] and Siberian Traps LIP [*Ivanov et al.*, 2008; *Ivanov and Litasov*, 2013; *Ivanov*, 2015]. Occurrence of the Haladala intrusion in an orogenic belt raises the possibility of subduction scenario for its generation. Clearly, further detailed characterization of the Haladala layered gabbroic intrusion is needed. In this study, we carried out detailed petrographic, geochemical, and geochronologic investigations on the Haladala intrusion. The aims were (1) to elucidate the magma sources, magma generation, and evolution processes, (2) to explore the possible linkage to the Tarim mantle plume, and (3) to clarify the effects and features of plume-orogenic lithosphere interaction.

2. Geological Setting and Sample Description

The Central Asian Orogenic Belt (CAOB) [*Zonenshain et al.*, 1990; *Jahn et al.*, 2000] or the Altaid Tectonic Collage (Altaids) [*Şengör et al.*, 1993], sandwiched between the Siberian and North China-Tarim-Karakum cratons (Figure 1a), is the largest Phanerozoic accretionary orogen in the world [*Windley et al.*, 2007; *Xiao et al.*, 2009a, 2009b]. The Chinese Tianshan Belt, located in the southwestern part of the CAOB, extends west-east for more than 2400 km from the Aral Sea eastward through Uzbekistan, Tajikistan, Kyrgyzstan, and Kazakhstan to Xinjiang in northwestern China, and separates the Tarim Basin to the south from the Junggar Basin to the north (Figure 1b). The Chinese Tianshan Belt has been divided into eastern and western segments along the Tuokexun-Kumishi High Road (at meridian 88°E) [*Ma et al.*, 1993]. The western segment of the Chinese Tianshan Belt is further divided into four tectonic units of the North Tianshan, Yili Block, Central Tianshan, and South Tianshan (Figure 1b) [*Huang et al.*, 1987; *Allen et al.*, 1992; *Gao et al.*, 2009]. The North Tianshan consists mainly of a west-northwest-striking ophiolitic mélange zone. The Yili Block is the eastern part of the Kazakhstan microcontinent and consists of Precambrian basement superimposed by Paleozoic volcanic and sedimentary rocks [*Gao et al.*, 2009]. The Central Tianshan is an arc terrane along the southern margin of the Yili Block as eastern extension of the Kyrgyzstan Middle Tianshan [*Gao et al.*, 2009; *Qian et al.*, 2009]. It is amalgamated with the Yili Block as a result of the closure of the "Terskey Ocean" during the Early Ordovician and is furthermore related to the subduction of the "South Tianshan Ocean" from Silurian to latest Carboniferous times [e.g., *Gao et al.*, 2009]. The South Tianshan was the collision zone between the Tarim and Yili blocks that resulted from closure of the South Tianshan Ocean during the Late Paleozoic. The South Tianshan Orogen has traditionally been considered to be a Paleozoic orogen that was reactivated during the Cenozoic [*Windley et al.*, 1990; *Yin et al.*, 1998]. There is much debate on the timing of the collision between the Tarim and Yili blocks [e.g., *Allen et al.*, 1992; *Bazhenov et al.*, 2003; *Gao et al.*, 1998, 2011; *Xiao et al.*, 2009a, 2009b]. Nevertheless, the geochronological data obtained for the Tianshan high-pressure/low-temperature metamorphic rocks and stitching granitic plutons suggest that the final collision took place in the Late Carboniferous (~320–300 Ma) [*Gao et al.*, 2011; *Han et al.*, 2011, and references therein].

The Haladala gabbroic pluton, located at northeast Tekex County, is one of the largest layered ultramafic-mafic intrusive complexes in the Southwest Tianshan Orogen (Figures 1b and 2a). It extends east-west with a length of ~13 km and width of ~2–3 km (Figure 1c) and has a total exposure area of approximately 25 km^2 [*Gao et al.*, 1991; *Zhang et al.*, 2000]. The pluton intruded concordantly into the Carboniferous volcanic and sedimentary sequence, contacting with the Lower Carboniferous Akeshake Formation (C_1a; Figure 1c) along its eastern, western, and southern sides and the Middle Carboniferous Yishijilike Formation (C_2y; Figure 1c) along its northern margin. The layered pluton consists of gabbro in the core and diabase toward the margin (Figure 1c). Some magnetite-rich pegmatitic layers with thickness of up to 1 m are present in the upper section of the pluton's layered sequence (Figures 2b and 2c). In this study, 16 samples for geochemical analyses (seven olivine-bearing samples and nine olivine-free samples; Table S1 in the supporting information) were collected along a valley penetrating the central-eastern part of the pluton (Figure 1c).

The olivine-bearing samples, including pyroxene troctolite and olivine gabbro (Figures 2d and 2e), consist dominantly of euhedral plagioclase (38–68%), clinopyroxene (8–47%), subhedral to anhedral olivine (3–26%), and minor anhedral Fe-Ti oxides (magnetite and ilmenite, <1–6%). The olivine-free gabbro (Figure 2f) consists mainly of euhedral plagioclase (34–66%), clinopyroxene (30–64%), and anhedral Fe-Ti oxides (<1–4% in the samples listed in Table S1 for bulk rock geochemical analyses, but 10–15% in some samples and more in the samples from the V-Ti magnetite-rich layers; Figure 2g). In the olivine-bearing samples, small olivines are enclosed by plagioclases, or some plagioclases are as inclusions in olivines (Figures 2d and 2e), suggesting simultaneous crystallization of the two minerals. Clinopyroxenes are interstitial to olivines and plagioclases in the pyroxene troctolite (Figure 2d) or are large and enclose olivines and plagioclases showing typically poikilitic texture (Figures 2e and 2f). Rare biotite (<< 1%) is present as anhedral crystals on the periphery of magnetite in some samples. Some plagioclases are partially altered to fine-grained mica-rich aggregates, while clinopyroxenes are mostly fresh. Fe-Ti oxide (magnetite and ilmenite) is interstitial to olivine, plagioclase, and/or clinopyroxene, but intergrowth with clinopyroxene in the pegmatitic sample (Figure 2g).

Magnetite grains usually contain ilmenite exsolution lamellae (Figure 3a). In addition to exsolution lamellae, ilmenite grains are dominantly interstitial to olivine or plagioclase with or without intergrowth relationship with magnetites (Figures 3b–3e). In general, the intergrowth of ilmenite and magnetite exhibits core and
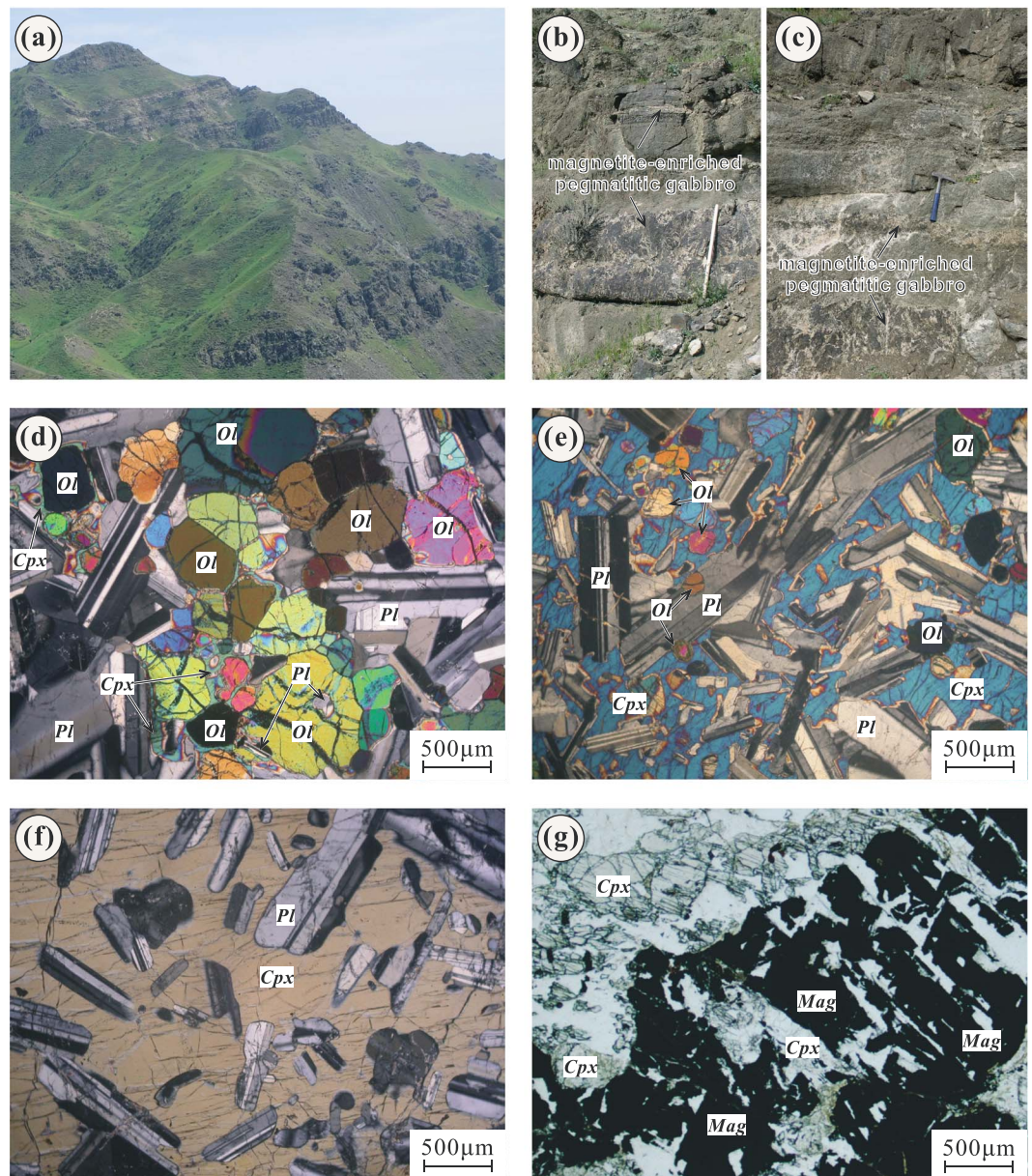
Figure 2. (a) Field photograph showing layered structure of the Haladala gabbros. (b and c) Outcrop of magnetite-enriched pegmatitic layers with thickness of up to 1 m in the upper section of layered sequence of the pluton. the length of white stick in Figure 2b is about 1 m, and that of the hammer in Figure 2c is 28 cm. (d) Micrography of pyroxene troctolite, minor clinopyroxene (Cpx) as interstitial phases between olivine (Ol) and plagiolcase (Pl) or surrounding olivine, and some fine-grained plagioclases enclosed within olivine (crossed-polarized light), (e) Micrography of olivine-bearing gabbro, rounded olivine enclosed within tabular plagioclase or anhedral clinopyroxene, and clinopyroxene as interstitial phases between tabular plagioclases (crossed-polarized light). (f) Micrography of olivine-free gabbro, large clinopyroxene encloses tabular plagioclases, showing typical poikilitic texture (crossed-polarized light). (g) Abundant anhedral magnetite (Mag) grains intergrowth with clinopyroxene in the pegmatitic gabbro of the upper layered of the intrusion (plane-polarized light).

rim texture that ilmenite is enclosed by magnetite (Figures 3c and 3d). Individual ilmenite grains are all irregular crystals filling the interspace between olivine and plagioclase or as inclusion of olivine (Figure 3e).

3. Analytical Methods

Zircons were separated using conventional heavy liquid and magnetic techniques and purified by handpicking under a binocular microscope. They were mounted in epoxy resin. The mount was polished to expose the
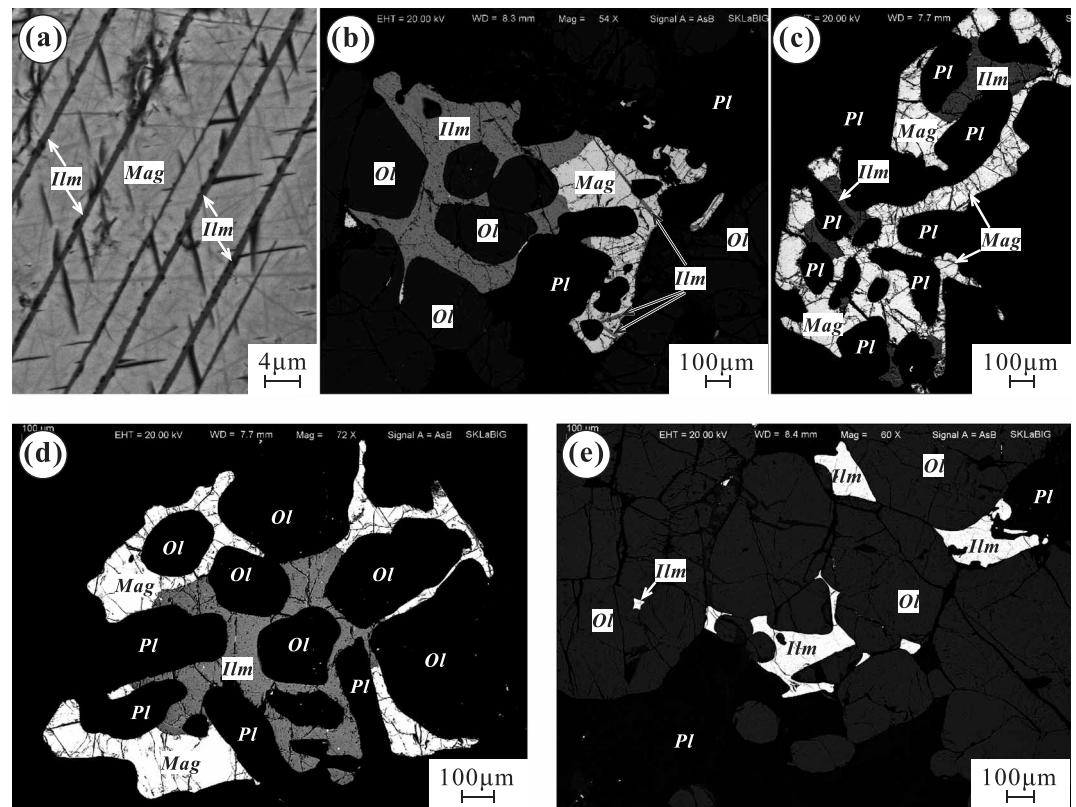
Figure 3. BSE images of the Haladala gabbros: (a) the exsolution lamellae of ilmenite (Ilm) within magnetite (Mag); (b) the intergrowth of magnetite (Mag) and ilmenite (Ilm); Ilm on the left is interstitial to Ol and Pl; magnetite (Mag) on the right contains the exsolution lamellae of ilmenite; (c, d) the intergrowth of magnetite and ilmenite exhibits core and rim texture; magnetite enclosing ilmenite that is interstitial to olivine and plagioclase; and (e) individual ilmenite grains are interstitial to olivine and plagioclase or as inclusion within olivine.

grain centers and then coated by gold. The internal structure of the zircons was examined using cathodoluminescence (CL) images prior to oxygen, U-Pb, and Lu-Hf isotopic analyses.

Sample TKS1155 was selected for zircon oxygen isotope analyses, which were performed on the Cameca IMS 1280 ion microprobe at the Institute of Geology and Geophysics, Chinese Academy of Sciences (IGG-CAS) in Beijing. The Cs^+ primary ion beam was accelerated at 10 kV, with an intensity of approximately 2 nA and rastered over a 10 μm area. The spot size is about 20 μm in diameter (10 μm beam diameter + 10 μm raster). Detailed analytical procedures are described by *Li et al.* [2010b]. The internal precision of a single analysis was generally better than 0.2‰ for $^{18}O/^{16}O$ ratio. $\delta^{18}O$ values are standardized to Vienna standard mean ocean water (VSMOW) compositions and reported in standard per mil notation. The instrumental mass fractionation factor is corrected using 91500 zircon standard with $(\delta^{18}O)_{VSMOW} = 9.9$‰ [*Wiedenbeck et al.*, 2004]. Measured $^{18}O/^{16}O$ is normalized using VSMOW and then corrected for the instrumental mass fractionation factor [*Li et al.*, 2010b]. Nine measurements of the Qinghu zircon standard during the course of this study yield a weighted mean of $\delta^{18}O = 5.44 \pm 0.22$‰ (95% confidence level), which is consistent within errors with the reported value of 5.4 ± 0.2‰ [*Li et al.*, 2013].

For comparison, samples TKS1155 and TKS13015 were selected for zircon U-Pb analyses using the Cameca IMS 1280 ion microprobes at IGG-CAS and Guangzhou Institute of Geochemistry, Chinese Academy of Sciences (GIG-CAS), respectively. The two laboratories adopted the same procedures for zircon U-Pb analyses, but the analyses of sample TKS1155 were carried out on the spots previously for oxygen isotopic analyses using the Cameca IMS 1280 ion microprobe at IGG-CAS. The O_2^- primary ion beam was accelerated at 13 kV, with an intensity of approximately 8 nA. The ellipsoidal spot is about 20×30 μm in size. Positive secondary ions were extracted with a 10 kV potential. Detail analytical procedures are similar to those described by *Li et al.* [2010b]. Pb/U calibration was performed relative to the 417 Ma standard zircon TEMORA 2 based

on an observed linear relationship between $\ln(^{206}Pb/^{238}U)$ and $\ln(^{238}U^{16}O_2/^{238}U)$. U-Th-Pb isotopic ratios and absolute abundances of unknowns were determined relative to the standard zircon 91500 [*Wiedenbeck et al.*, 1995]. Measured Pb isotopic compositions were corrected for common Pb using the measured ^{204}Pb. An average of present-day crustal composition [*Stacey and Kramers*, 1975] is used for the common Pb assuming that it is largely due to surface contamination induced during sample preparation. The common-Pb corrections were insensitive to the choice of common-Pb compositions due to the high ratios (mostly > 10000) of our measured zircon $^{206}Pb/^{204}Pb$ (Table S2). Uncertainties on individual analyses are reported at the 1σ level, and data reduction was carried out using Isoplot (version 3.23) [*Ludwig*, 2003].

Zircon Hf isotopic analyses of TKS1155 were carried out on the spots previously for O and U-Pb isotopic analyses using laser ablation multicollector inductively coupled plasma mass spectrometry (LA-MC-ICP-MS) at GIG-CAS. Spot size of 45 μm with a laser repetition rate of 8 Hz was used, with an energy density of 80 mJ. ^{173}Yb and ^{175}Lu were used to correct the isobaric interference of ^{176}Yb and ^{176}Lu on ^{176}Hf. Due to the extremely low $^{176}Lu/^{177}Hf$ in zircon (normally < 0.002 in the studied sample, Table S3), the isobaric interference of ^{176}Lu on ^{176}Hf is negligible [*Iizuka and Hirata*, 2005]. No obvious relationship between $^{176}Yb/^{177}Hf$ and $^{176}Hf/^{177}Hf$ ratios was observed in the studied sample, indicating that the correction of ^{176}Yb interference on ^{176}Hf is precise for obtaining accurate $^{176}Hf/^{177}Hf$ values. The $^{176}Hf/^{177}Hf$ was normalized to $^{179}Hf/^{177}Hf$ (0.7325) using an exponential law for mass bias correction. Eight Penglai zircons were used as the reference standard [*Li et al.*, 2010c], which yield a weighted mean $^{176}Hf/^{177}Hf$ of 0.282905 ± 0.000014 (95% confidence level). This is consistent with the reference value of $^{176}Hf/^{177}Hf = 0.282906 \pm 0.000010$ [*Li et al.*, 2010c]. Details of Hf isotopic analytical method are similar to those described by *Wu et al.* [2006].

Geochemical and Sr-Nd-Pb-Hf isotopic analyses were all carried out at the State Key Laboratory of Isotope Geochemistry, GIG-CAS. Samples were sawed into slabs, and the central parts (>200 g) were used for bulk rock analyses. The rocks were crushed into small fragments (<0.5 cm in diameter) before further cleaned with deionized water in an ultrasonic bath and powdered in a corundum mill.

Bulk rock major element oxides were analyzed using a Rigaku RIX 2000 X-ray fluorescence spectrometer. Calibration lines used in quantification were produced by bivariate regression of data from 36 reference materials encompassing a wide range of silicate compositions. Calibrations incorporated matrix corrections based on the empirical Traill-Lachance procedure, and analytical uncertainties are mostly between 1% and 5%. Trace elements were analyzed using inductively coupled plasma mass spectrometry (ICP-MS) after acid digestion of samples in high-pressure Teflon vessels. An internal standard solution containing the single element Rh was used to monitor signal drift. The U.S. Geological Survey and Chinese National standards GSR-1, GSR-2, GSR-3, G-2, W-2, BT142, AGV-2, MRG-1, and ROA-1 were chosen for calibrating element concentrations of the analyzed samples. Analytical precision of rare earth element (REE) and other incompatible elements is typically 1–5%.

Sr-Nd-Pb-Hf isotopic ratios were measured on a subset of whole rock samples using a Neptune Plus multicollector ICP-MS (MC-ICP-MS). The Sr-Nd isotopic analytical methods follow the procedure of *Wei et al.* [2002] and *Liang et al.* [2003]. Normalizing factors used to correct the mass fractionation of Sr and Nd during the measurements are $^{86}Sr/^{88}Sr = 0.1194$ and $^{146}Nd/^{144}Nd = 0.7219$. Reference standards were analyzed along with samples and give $^{87}Sr/^{86}Sr = 0.710269 \pm 6$ (2σ, the last digit) for NBS987 and $^{143}Nd/^{144}Nd = 0.512093 \pm 4$ (2σ) for Shin Etsu JNdi-1 (0.512115 ± 5 [*Tannaka et al.*, 2000]).

For Hf isotope analysis, the mixture of about 100 mg rock powder and 200 mg $Li_2B_4O_7$ was fused in a Pt-Au alloy crucible at 1200°C for 15 min in a high-frequency furnace. The quenched piece of alkali glass was dissolved in 2 mol/L HCl. Hf fraction was separated by using a modified single-column Ln extraction chromatography method. The measured $^{176}Hf/^{177}Hf$ ratios were normalized to $^{179}Hf/^{177}Hf = 0.7325$, and the reported $^{176}Hf/^{177}Hf$ ratios were further adjusted relative to the standard JMC-475 of 0.282160. Reference standard was analyzed along with samples and give $^{176}Hf/^{177}Hf = 0.282191 \pm 3$ (2σ) for JMC475.

For Pb isotope measurements, 100 mg of rock powder was weighed into a Teflon vessel and dissolved in a HNO_3+ HF mixture at 140°C for 72 h. The solution was evaporated to dryness and then added with 2 mL concentrated HNO_3 and kept on a hot plate at 140°C for 24 h. It was evaporated to dryness again and subsequently added with 2 mL 6 M HCl and kept on a hot plate at 140°C for another 24 h. It was finally dissolved in 0.8 M HBr solution in preparation for Pb purification. Pb was separated and purified by conventional anion
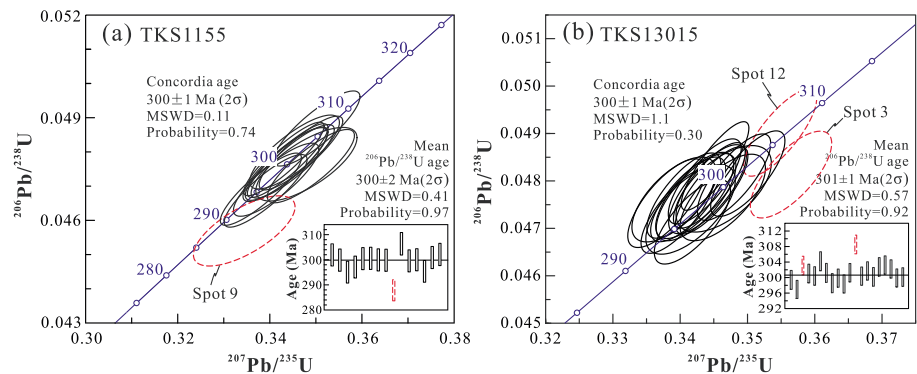
Figure 4. Concordia diagrams for secondary ion mass spectrometry (SIMS) zircon U-Pb analyses of the Haladala layered gabbroic intrusion. (a) Sample TKS1155 and (b) sample TKS13015.

exchange techniques (AG1X8, 200–400 resin) with dilute HBr as eluant. The total procedural blank is less than 0.4 ng. Samples are doped with Tl, and mass discrimination was corrected relative to a certified $^{205}Tl/^{203}Tl$ ratio. The detail analytical procedures are similar to those described by *Baker and Waight* [2002]. During the period of analysis, repeated analyses of National Institute of Standards and Technology Standard Reference Material 981 yielded $^{206}Pb/^{204}Pb = 16.9368 \pm 4$ (2σ), $^{207}Pb/^{204}Pb = 15.4881 \pm 5$ (2σ), and $^{208}Pb/^{204}Pb = 36.6788 \pm 11$ (2σ).

Backscattered electron (BSE) images were carried out using a Carl Zeiss SUPRA55SAPPHIRE field emission-scanning electron microscope at GIG-CAS. Major element analysis of minerals was obtained by electron microprobe analysis using a JEOL JXA-8100 SuperProbe. The operating conditions are 15 kV accelerating voltage, 20 nA beam current, and 1–2 μm beam diameter. A variable peak counting time of 7–40 s was used depending on the intensity of characteristic X-ray line and desired precision. The data reduction was carried out using atomic number, absorption and fluorescence (ZAF) correction. Used standards were magnetite (Fe), rutile (Ti), metal vanadium (V), metal nickel (Ni), Cr_2O_3 (Cr), MnO (Mn), diopside (Mg), plagioclase (Si, Al, Na, and Ca), and orthoclase (K).

In situ trace element analyses of magnetite and ilmenite grains from the Haladala gabbros were made by laser ablation inductively coupled plasma mass spectrometry (LA-ICP-MS) at GIG-CAS, using an Agilent 7500a ICP-MS system coupled with a Resolution M50-HR 193 nm ArF-excimer laser sampler. The analytical procedure was described by *Tu et al.* [2011]. Spot diameter of 80 μm and repetition rate of 10 Hz were applied to the analyses. Ablation signal and integration intervals were carefully selected by reviewing the time-resolved analysis to make sure there were no inclusions present in the analyzed volume. The results were acquired using the commercial software ICPMSDataCal 6.7 [*Liu et al.*, 2008]. Calibration was carried out externally using KL2 and ML3B with Fe as an internal standard. Repeated analyses of KL2 and ML3B indicate that both precision and accuracy are better than 5% for most elements. For ilmenite, the relative standard deviations (RSDs) of Nb, Ta, Zr, and Hf are better than 4%, and those of REE vary from 3–30% for high-concentration elements to 30–50% for low-concentration ones. For magnetite, the RSDs of high-concentration elements are 3–15%, and those of low-concentration elements are 15–50%.

4. Analytical Results

4.1. In Situ Zircon U-Pb Geochronology and Hf-O Isotopes

Zircons from sample TKS1155 are all fragments due to overcrushing, while those from sample TKS13015 are mostly euhedral and elongate to stubby. CL images show well-developed oscillatory zoning, indicating a magmatic origin.

Zircons of sample TKS1155 have moderate Th and U contents (71–512 ppm and 213–670 ppm, respectively) with variable Th/U ratios of 0.32–1.02 (Table S2). Except for Spot 9 with an exceptionally young $^{206}Pb/^{238}U$ age due to extremely high $^{206}Pb/^{204}Pb$ ratio (Table S2), the U-Pb results form a coherent cluster and yield a concordia age of 300 ± 1 Ma (mean square weighted deviation (MSWD) = 0.11) and a mean $^{206}Pb/^{238}U$ age of 300 ± 1 Ma (MSWD = 0.41; Figure 4a).

Twenty zircons from sample TKS13015 have moderate to high Th and U contents (110–1540 ppm and 216–602 ppm, respectively) with variable Th/U ratios of 0.40–2.80 (Table S2). Spot 3 is slightly discordant but has apparent $^{206}Pb/^{238}U$ age of 303 ± 2 Ma, and spot 12 has slightly old apparent $^{206}Pb/^{238}U$ age of 309 ± 2 Ma (2σ; Table S2). Except for Spots 3 and 12, the U-Pb results form a coherent cluster and yield a concordia age of 300 ± 1 Ma (2σ; MSWD = 1.1) and a weighted mean $^{206}Pb/^{238}U$ age of 301 ± 1 Ma (2σ; MSWD = 0.57; Figure 4b).

The dates obtained from two laboratories are identical within errors, interpreted as the crystallization age of the Haladala gabbro. These ages are slightly younger than the previous dates of 306 ± 2 Ma [*Zhu et al.*, 2010] and 309 ± 2 Ma [*Xue and Zhu*, 2009].

Zircons from sample TKS1155 have similar and high $^{176}Hf/^{177}Hf$ ratios (0.282842–0.282970), corresponding to high positive $\varepsilon_{Hf}(t)$ values (8.3–13.1; Table S3 and Figure S1). The single-stage Hf model ages range from 398 Ma to 595 Ma (Table S3), which are slightly older than the crystallization age of ~300 Ma. The corresponding $\delta^{18}O$ values are quite homogeneous (5.69‰ to 6.64‰ with mean value of 6.3 ± 0.3‰; Table S3 and Figure S1) and slightly higher than the values of mantle-derived zircons (5.3 ± 0.3‰) [*Valley et al.*, 1998].

4.2. Major and Trace Elements

Bulk rock analyses of 16 samples of the Haladala intrusion show wide variations in major element compositions (Table S4). They have moderate to high MgO (5.22–14.59 wt %), Fe_2O_3 (6.70–14.15 wt %), and CaO (8.65–15.66 wt %), moderate TiO_2 (0.57–2.65 wt %) and Na_2O (2.05 − 4.28 wt %), but low SiO_2 (45.65–50.66 wt %), P_2O_5 (0.05–0.28 wt %), and K_2O (0.18–1.10 wt %). The total alkalis ($Na_2O + K_2O$) vary in the range of 2.23–5.00 wt % (Table S4). The Na_2O/K_2O ratios are high and variable (2.97–11.39), indicating their low-potassium and high-sodium nature. For the olivine-bearing samples, TKS1160 and TKS1161 have relatively higher K_2O (0.46 wt % and 0.72 wt %, respectively; Table S4) than others (0.18–0.33 wt %; Table S4) due to heavy alteration (e.g., larger loss on ignition (LOI) of 2.24 and 1.98, respectively; Table S4). The olivine-free samples have overall higher Na_2O, K_2O, TiO_2, and CaO/Al_2O_3 than the olivine-bearing samples, except for altered samples (TKS1160 and TKS1161; Figures 5a–5d) that are also accumulation with Fe-Ti oxides (4% and 6%, respectively; Table S1). All samples show positive correlations between MgO and Ni (Figure 5e). The olivine-free samples exhibit positive correlations between V, TiO_2, and Fe_2O_3 (Figures 5c and 5f).

The Haladala gabbros also have extremely variable trace element concentrations. The rocks show slightly fractionated chondrite-normalized REE patterns ([La/Yb]$_N$ = 1.14–2.70), with weak negative to positive Eu anomalies (0.88–1.41) in olivine-free samples and all positive Eu anomalies (1.08–1.41) in the olivine-bearing samples (Figure 6a and Table S4). On a primitive mantle-normalized multielement variation diagram (Figure 6b), the Haladala gabbros have overall flat patterns compared to ocean island basalts (OIB)-like picrites and basalts emplaced in the Tarim Basin [*Tian et al.*, 2010] and are characterized by moderate negative Nb-Ta anomalies and positive Pb anomaly, with positive Sr anomaly and weak Ti anomaly (Figure 6b).

4.3. Bulk Rock Sr-Nd-Pb-Hf Isotopes

The Haladala gabbros exhibit narrow ranges of $^{87}Sr/^{86}Sr$, $^{143}Nd/^{144}Nd$, and $^{176}Hf/^{177}Hf$ ratios (Table S5). They are characterized by low initial $^{87}Sr/^{86}Sr$ (0.7038–0.7050) and high positive $\varepsilon_{Nd}(t)$ (+3.8 to +5.7) and $\varepsilon_{Hf}(t)$ (+10.3 to +14.6). On the conventional Sr-Nd isotope diagram (Figure 7a), the Haladala gabbros plot in the field of ocean island basalts (OIB), similar to the third episode (~280 Ma) of Permian Tarim mafic magmatism. Isotopically, they are more depleted than the second episode (~290 Ma) of Tarim Permian mafic magmatism (Figure 7a). The bulk rock Nd-Hf isotopic compositions for the Haladala gabbros plot within the fields of oceanic basalts or island arc volcanics but slightly above the mantle array line (Figure 7b) [*Chauvel et al.*, 2008], showing weak decoupling ($\Delta\varepsilon_{Hf}$ = 2.5–6.0). In comparison, the ~280 Ma Tarim LIP magmas are close to or below the line (Figure 7b).

The Haladala gabbros have a narrow range of $^{206}Pb/^{204}Pb$, $^{207}Pb/^{204}Pb$, and $^{208}Pb/^{204}Pb$ ratios (Table S6). They all display high initial $^{207}Pb/^{204}Pb$ (15.571–15.538) and $^{208}Pb/^{204}Pb$ (38.190–38.876) relative to mid-ocean ridge basalt (MORB)-like initial $^{206}Pb/^{204}Pb$ (17.986–18.368) and plot above the Northern Hemisphere Pb reference line (NHRL) [*Hart*, 1984] (Figures 7c and 7d). Such Pb isotopic characteristics are generally classified as the DUPAL anomaly [*Hart*, 1984; *Hawkesworth et al.*, 1986; *Castillo*, 1988; *Huang et al.*, 2013]. In comparison with the Tarim Permian mafic rocks, the Haladala gabbros have overall higher
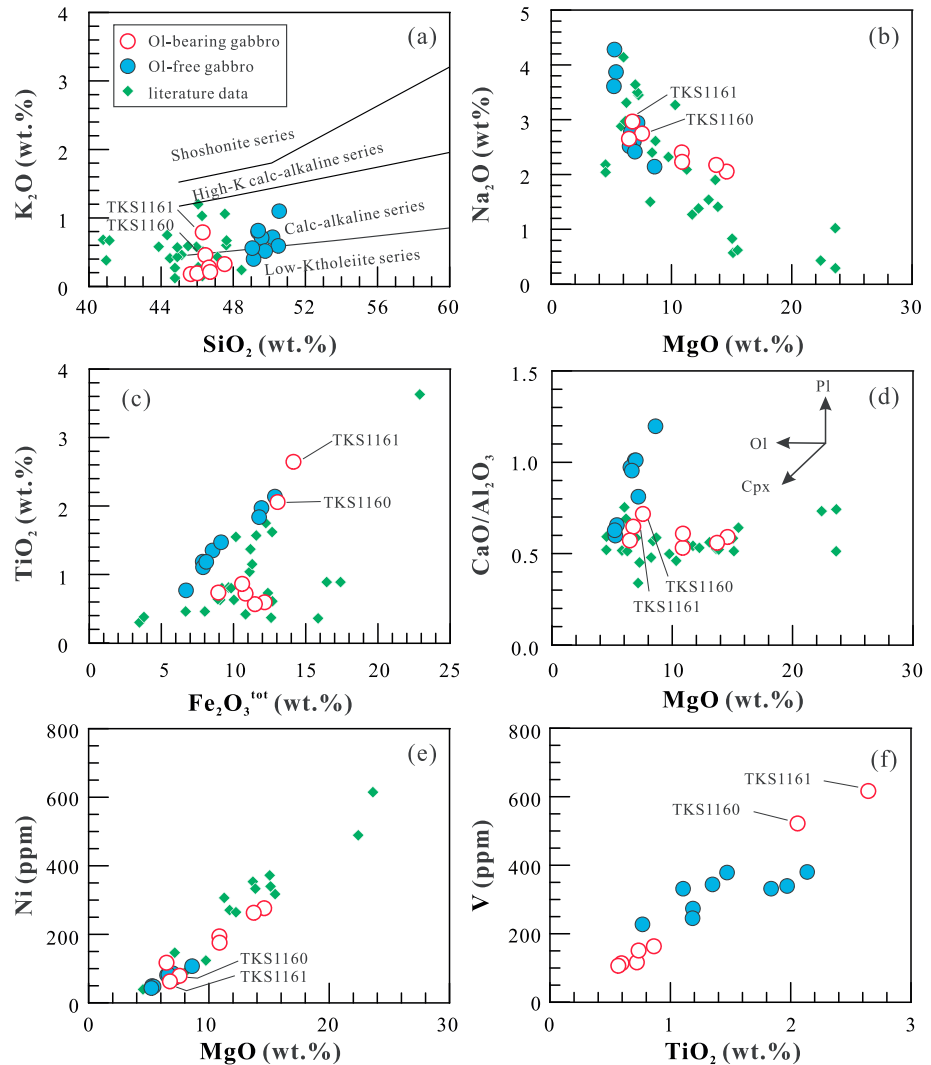
Figure 5. Variation diagrams for representative major element oxides and minor elements of the Haladala layered gabbroic intrusion: (a) K_2O versus SiO_2; (b) Na_2O versus MgO; (c) TiO_2 versus Fe_2O_3; (d) CaO/Al_2O_3 versus MgO; (e) Ni versus MgO; and (f) V versus TiO_2. The subdivision of subalkalic rocks using the K_2O versus silica is after *Rickwood* [1989]; the arrows on the CaO/Al_2O_3 versus MgO diagram denote the evolution trend of fractional crystallization of plagioclase (Pl), olivine (Ol), or clinopyroxene (Cpx); literature data of the Haladala layered gabbroic intrusion [*Xue and Zhu*, 2009; *Zhu et al.*, 2010; *Long et al.*, 2012] are shown for comparison.
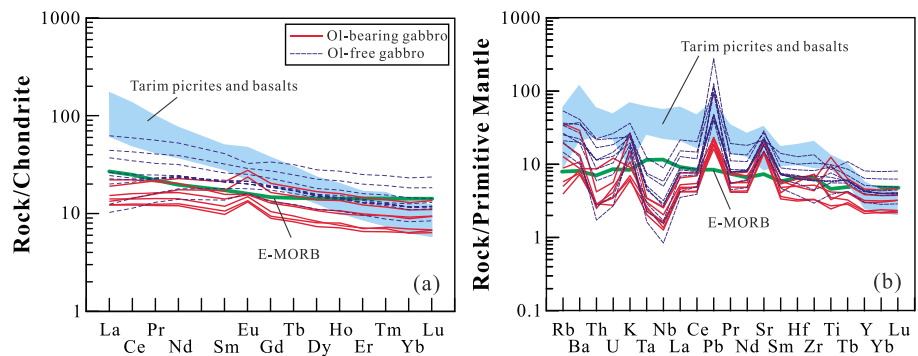
Figure 6. (a) Chondrite-normalized REE patterns and (b) primitive mantle-normalized multielement diagrams of the Haladala gabbroic intrusion. Normalization values and data of E-MORB are from *Sun and McDonough* [1989]. The Tarim picrites and basalts are from *Tian et al.* [2010].
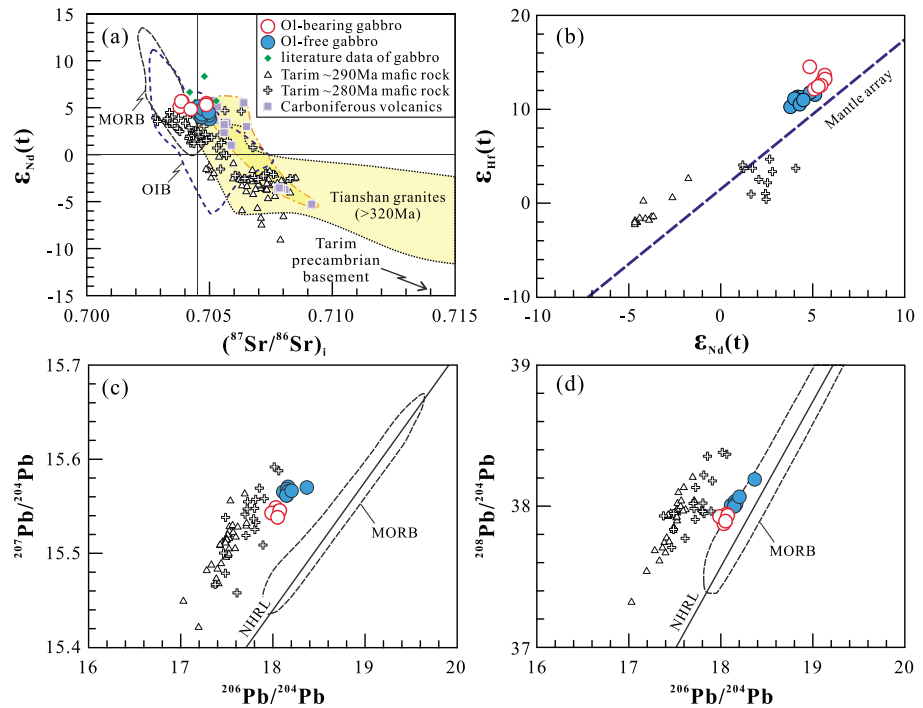
Figure 7. Sr-Nd-Hf-Pb isotopes of the Haladala gabbroic intrusion. (a) $\varepsilon_{Nd}(t)$ versus $(^{87}Sr/^{86}Sr)_i$; (b) $\varepsilon_{Hf}(t)$ versus $\varepsilon_{Nd}(t)$; Nd-Hf mantle array with relationship of $\varepsilon_{Hf} = 1.59\varepsilon_{Nd} + 1.28$ is from *Chauvel et al.* [2008]; the fields of oceanic basalts and island arc volcanics are from *Vervoort et al.* [2011] and references therein; (c and d) $^{207}Pb/^{204}Pb$ versus $^{206}Pb/^{204}Pb$ and $^{208}Pb/^{204}Pb$ versus $^{206}Pb/^{204}Pb$. Northern Hemisphere Reference Line (NHRL) and mantle source of MORB are from *Zindler and Hart* [1986]. Sr-Nd isotopic data sources: the Paleozoic granites of >320 Ma in Southwest Tianshan [*Gao et al.*, 2009; *Gou et al.*, 2012; *Long et al.*, 2011, and reference therein] and the Haladala gabbros [*Long et al.*, 2012, this study]. Sr-Nd-Pb-Hf isotopic data of Tarim mafic rock and Sr-Nd isotopic data of Carboniferous volcanic and sedimentary sequence (Dahalajunshan Formation) were from literatures [*Cao et al.*, 2014; *Ge et al.*, 2015; *Jiang et al.*, 2004, 2006; *Li et al.*, 2012c, 2014; *Sun et al.*, 2007, 2008; *Tian et al.*, 2010; *Wei and Xu*, 2011; *Wei et al.*, 2014; *Yu et al.*, 2011, 2012; *Zhang et al.*, 2010c, 2012; *Zhou et al.*, 2009; *Zhu et al.*, 2009]. The initial Sr-Nd-Hf-Pb isotopes were all calculated at 300 Ma.

$^{206}Pb/^{204}Pb$ with the similar or slightly higher $^{207}Pb/^{204}Pb$ and $^{208}Pb/^{204}Pb$ and define a variation trend more close to the NHRL (Figures 7c and 7d).

4.4. Magnetite and Ilmenite Compositions

All the magnetites contain relatively high TiO_2 (6.0–11.7 wt %) and V_2O_3 (0.90–1.18 wt %) (Table S7), corresponding to V-Ti magnetite [*He et al.*, 2013]. Total REE contents of magnetite and ilmenite vary from 1.49 ppm to 34.26 ppm (Table S7). Ilmenite contains high Nb, Ta, Zr, and Hf with high [Nb/La]$_{PM}$, [Nb/Zr]$_{PM}$ and Nb/Ta relative to magnetite (Table S7). Specifically, [Nb/La]$_{PM}$ values of measured ilmenites are remarkably high (485–4211; Table S7), and Nb/Ta ratios vary from 11.6 to 20.7 (Table S7) with a mean value of ~16.0 that is slightly lower than the C1 chondritic value of 17.6 [*Sun and McDonough*, 1989].

5. Discussion

5.1. Emplacement Age of the Haladala Gabbros

Previous zircon U-Pb dating results suggest that the Haladala intrusion was emplaced during the Late Carboniferous ($306 \pm 2 \sim 309 \pm 2$ Ma) [*Xue and Zhu*, 2009; *Zhu et al.*, 2010], predating the magmatism of the Tarim LIP (300–280 Ma) [*Zhang et al.*, 2013; *Xu et al.*, 2014]. The zircon U-Pb ages obtained in this study are all slightly younger than the previous dates [*Xue and Zhu*, 2009; *Zhu et al.*, 2010]. It is therefore necessary to inspect the details of these published data. *Xue and Zhu* [2009] obtained the emplacement age of the Haladala gabbros using zircon Sensitive High Resolution Ion Microprobe (SHRIMP) II U-Pb dating technique. However, their reported $^{207}Pb/^{235}U$ ratio and apparent $^{206}U/^{238}Pb$ age all have large errors of 2.5–9.3% and 3.1–4.4%, respectively [*Xue and Zhu*, 2009]. In addition, the analyses by *Xue and Zhu* [2009] are mostly

discordant and can only yield a mean $^{206}Pb/^{238}U$ age of 309 ± 2 Ma. *Zhu et al.* [2009] obtained the age using Cameca IMS-1280 ion microprobe similar to this study. However, these analyses also gave large errors for the isotope ratios (1.9–6.5% for $^{207}Pb/^{235}U$ ratio and $>$ 1.5% for $^{206}Pb/^{238}U$ ratio [*Zhu et al.*, 2010]) and apparent ages (5.2–16.3% for $^{207}Pb/^{235}U$ age and 4.5–5.1% for $^{206}Pb/^{238}U$ age [*Zhu et al.*, 2010]), which yielded a mean $^{206}Pb/^{238}U$ age of 306 ± 2 Ma based on a wide range of apparent $^{206}Pb/^{238}U$ ages (296–316 Ma).

The analyses of samples TKS1155 and TKS13015 of this study have much lower errors for both U/Pb isotopes and apparent ages ($<$ 1.5%; 1σ; Table S2) compared to the previous data [*Xue and Zhu*, 2009; *Zhu et al.*, 2010]. Furthermore, these analyses are mostly concordant and yield the concordant ages that are identical to the mean $^{206}Pb/^{238}U$ ages (Figure 4), and the analyses performed in different laboratories yield virtually the same results. Therefore, the zircon U-Pb dating results of this study are considered superior to those previously published dates.

The emplacement age of the Haladala layered intrusion seems to be younger than the collision between the Tarim craton and Yili block (~320–300 Ma [*Gao et al.*, 2011; *Han et al.*, 2011, and references therein]) but is identical to the Wajilitag kimberlite (~300 Ma [*Zhang et al.*, 2013]). The latter was interpreted as the earliest phase of magmatism of the Tarim mantle plume [*Zhang et al.*, 2013; *Xu et al.*, 2014].

5.2. Fractional Crystallization and Accumulation

Layered intrusions are generally associated with the evolution of large magmatic systems including magma differentiation and magma chamber processes [e.g., *McBirney*, 1995; *Bédard*, 2001; *Barnes et al.*, 2004; *Tollari et al.*, 2008]. In the Haladala case, the wide variation in major and trace element compositions suggests that their parental melts may have experienced varying degrees of fractional crystallization and/or crystal accumulation. The correlations between CaO/Al_2O_3, Ni and MgO (Figures 5d and 5e) point to fractionation/accumulation of clinopyroxene and olivine, respectively. Specifically, the high-Mg samples (MgO $>$ 9 wt %) may have been subjected to olivine-dominated fractionation/accumulation, given the positive correlation between Ni and MgO (Figure 5e), but nearly constant CaO/Al_2O_3 ratios (Figure 5d). Clinopyroxene-dominated fractionation/accumulation is inferred for the samples with MgO $<$ 9 wt %, given the positive correlation between CaO/Al_2O_3 and MgO (Figure 5d). The samples with higher Eu/Eu* have overall lower REE, Th, and U concentrations than the samples with low Eu/Eu* (Table S4), which indicates variable extents of plagioclase fractionation/accumulation [*Huang et al.*, 2012]. Positive Eu anomalies on the REE patterns of the Haladala gabbros manifest distinct effects of plagioclase accumulation (Figure 6a).

The strong correlations between $Fe_2O_3^{tot}$, TiO_2, and V within the olivine-free samples of the Haladala pluton (Figures 5c and 5f) indicate Fe-Ti oxide fractionation/accumulation. The formation of magnetite layers (Figures 2b and 2c) in the upper section of the Haladala layered gabbros can be attributed to progressive enrichment of Fe and Ti in the residual melts through extensive fractionation of silicate minerals such as olivine, clinopyroxene, and plagioclase. In addition, magnetite is interstitial to olivine, plagioclase, and clinopyroxene or present on the periphery of ilmenite (Figures 3b and 3d), suggesting that it is the later phase of fractional crystallization. Oxygen fugacities calculated based on magnetite-ilmenite equilibration are lower than the nickel-nickel oxide buffer and mostly lower than the fayalite-magnetite-quartz buffer [*He et al.*, 2013], ensuring that Fe contents in magmas increased along with magma fractionation and finally resulted in the formation of the magnetite-enriched layers. However, most olivine-bearing samples have relatively low and constant TiO_2 and V (except for the samples of TKS1160 and TKS1161 that are accumulation with Fe-Ti oxides; Table S1), suggesting that the ilmenite may have been oversaturated and fractionated during earlier magma evolution. A peculiar petrographic feature supports this interpretation: ilmenite is always interstitial to olivine and plagioclase as a late phase in the troctolite mineral assemblage (Figures 3b and 3e). Additionally, olivine in the studied samples exhibits relatively low magnesium contents (Fo = 65–73 [*He et al.*, 2013]), suggesting an evolved nature for the rocks in outcrop that had undergone extensive olivine fractional crystallization.

5.3. Nb-Ta Depletion and Formation of an Enriched Mantle Source

The Haladala gabbros have moderate depletion in Nb and Ta, with low [Nb/La]$_{PM}$ values (0.24–0.41; Table S4). The origin of such geochemical features could be related to crustal contamination during magma ascent [e.g., *Kelemen et al.*, 1993; *Turner et al.*, 1999; *Barth et al.*, 2000], the hybridization in the mantle source by recycled terrigenous sediments [e.g., *Peccerillo*, 1985; *Hawkesworth et al.*, 1993; *Huang et al.*, 2012], suprasubduction

zone fluid metasomatism [e.g., *Tatsumi*, 1986; *Donnelly et al.*, 2004], or Ti-bearing minerals (such as rutile, ilmenite, and Ti-bearing amphibole) crystallization or retention in the source region [e.g., *Ionov and Hofmann*, 1995; *Huang et al.*, 2010; *Dygert et al.*, 2013].

5.3.1. Crustal Contamination

Crustal contamination is a potential process for mantle-derived melts during their ascent through continental crust or their evolution within a magma chamber in a continental environment. The Haladala gabbros are characterized by negative Nb and Ta anomalies but positive Pb anomaly on a primitive mantle-normalized multielement diagram, similar to those of the continental crust. Moreover, the initial $^{87}Sr/^{86}Sr$ ratios increase and $\varepsilon_{Nd}(t)$ and $\varepsilon_{Hf}(t)$ values decrease roughly with increasing SiO_2 and decreasing MgO in the Haladala gabbros (Figure S2), which are apparently consistent with crustal contamination processes. Relatively high zircon $\delta^{18}O$ values of the Haladala gabbros ($\delta^{18}O = 5.69–6.64‰$; Table S3) also indicate crustal contribution. K_2O content of the Haladala gabbros may have been significantly elevated by crustal contamination based on its positive correlation with initial $^{87}Sr/^{86}Sr$ ratios and negative relationship with $\varepsilon_{Nd}(t)$ and $\varepsilon_{Hf}(t)$ values (Figure S2), which means the primary melt was essentially very low in potassium. It is noteworthy that the olivine-free samples overall have lower $\varepsilon_{Nd}(t)$ and $\varepsilon_{Hf}(t)$ values but higher initial $^{87}Sr/^{86}Sr$ ratios than the olivine-bearing samples, consistent with increasing crustal contamination during the magma evolution. However, the two sample types show similar Nb/La and Nb/Ta ratios, indicating that the depletion of Nb and Ta in the Haladala grabbros was independent of crustal contamination.

The country rocks of the intrusion (e.g., Lower and Middle Carboniferous Formations; Figure 1c) and deep crustal materials (e.g., Paleozoic granites of >320 Ma and their crustal source in the southwest Tianshan area) are the main potential contaminants (Figures 7a and S2). Both the volcanic rocks within the Carboniferous sequence and the Paleozoic granites of > 320 Ma in the southwest Tianshan area show relatively higher $^{87}Sr/^{86}Sr$ ratios and broader but overall lower $\varepsilon_{Nd}(t)$ values than the Haladala gabbros (Figures 7a and S2). However, they have similar or even higher Nb/La ratios in comparison with the Haladala gabbros, indicating that the crustal contamination cannot be completely responsible for the depletion of Nb and Ta in the latter. In addition, very low potassium but high-sodium concentrations in the Haladala gabbros are not consistent with significant crustal contamination. Therefore, crustal contamination in a magma chamber may have contributed slightly to the magmatic evolution of the Haladala gabbros, but it cannot fully account for their Nb and Ta depletions.

5.3.2. Effect of Ti-Bearing Minerals

Both suprasubduction zone fluid metasomatism and Ti-bearing minerals crystallization or retention in the source region would cause significant depletion of Nb-Ta and Ti in the melts [e.g., *Tatsumi*, 1986; *Ionov and Hofmann*, 1995; *Donnelly et al.*, 2004; *Huang et al.*, 2010]. Suprasubduction zone fluid is extremely enriched in large ion lithophile elements (LILEs) because of the dehydration of the subducted oceanic crust but strongly depleted in Nb-Ta and Ti due to the retention of rutile in the residue. The lack of hydrous minerals (e.g., hornblende, biotite, or phlogopite) in the Haladala gabbros indicates a relatively dry magma source. The dry condition is consistent with low oxygen fugacity of the system [*He et al.*, 2013] and earlier crystallization of plagioclase relative to clinopyroxene (Figures 2d–2f), but not with fluid metasomatism associated with subduction processes. Rutile from ancient metasomatized subcontinental lithospheric mantle has superchondritic Nb/Ta ratios, but those from undisturbed residues would have subchondritic Nb/Ta ratios [*Aulbach et al.*, 2008]. Removal of rutile with subchondritic Nb/Ta ratios may cause high Nb/Ta ratios in the residual melts [e.g., *Huang et al.*, 2010]. The subchondritic Nb/Ta ratios (9.0–13.5; Table S4) and positive correlation between Nb/Ta and [Nb/La]$_{PM}$ for the Haladala therefore argue against the role of rutile (Figure 8a). The relatively high Dy/Yb ratios (1.72–2.00; Table S4) are also inconsistent with the trend expected for amphibole fractionation during magma evolution or retention in the mantle source.

Ilmenite is highly incompatible for REEs but compatible for Nb and Ta with similar partition coefficients for these two elements [e.g., *Green and Pearson*, 1987; *Klemme et al.*, 2006; *Dygert et al.*, 2013], suggesting that ilmenite fractionation can generate low Nb/La ratios but mostly preserve Nb/Ta ratios in the residual melts. The Haladala ilmenites contain high Nb and Ta and exhibit extremely high [Nb/La]$_{PM}$ values and near chondritic Nb/Ta ratios (Table S7), indicating that the crystallization of ilmenite during the earlier magma evolution may have been partially responsible for Nb-Ta depletion of the Haladala gabbros. In fact, the Haladala ilmenite is usually an interstitial phase in the troctolite mineral assemblage (Figures 3b–3e) that is earlier than
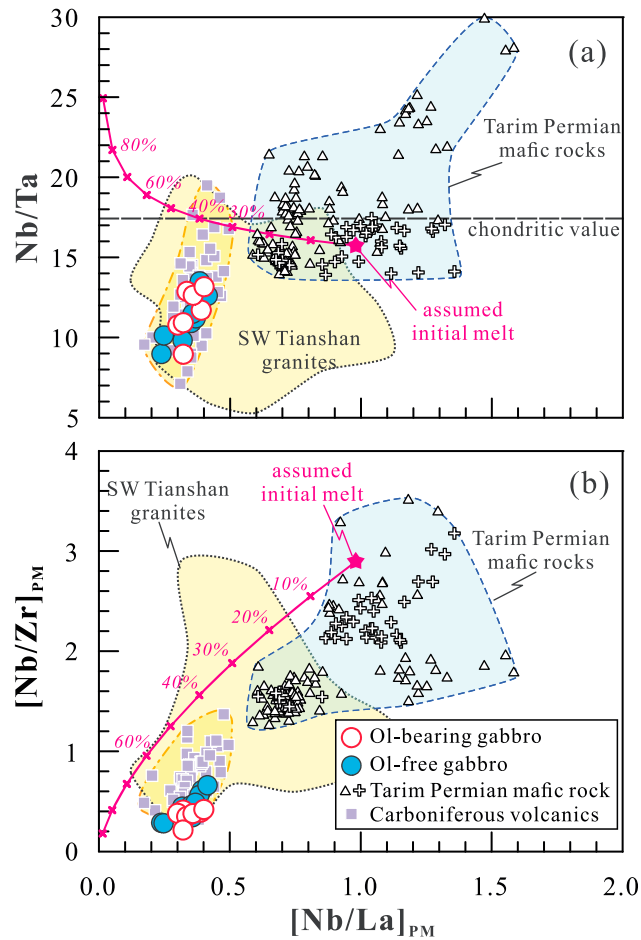
Figure 8. (a) Nb/Ta versus [Nb/La]$_{PM}$; and (b) [Nb/Zr]$_{PM}$ versus [Nb/La]$_{PM}$ for the Haladala gabbroic intrusion. The assumed mantle source is mean value of the picrites from Tarim LIP [*Tian et al.*, 2010]. Partition coefficients of ilmenite for La, Nb, Ta and Zr are from *Dygert et al.* [2013]. Literature data of Tarim Permian LIP mafic rocks [*Jiang et al.*, 2006; *Li et al.*, 2012b; *Tian et al.*, 2010; *Wei et al.*, 2014; *Yu et al.*, 2011; *Yuan et al.*, 2012; *Zhang et al.*, 2010a, 2010c; *Zhou et al.*, 2009] and Carboniferous volcanics [*Li et al.*, 2010a; *Liu et al.*, 2006; *Luo et al.*, 2009; *Ge et al.*, 2015; *Zhu et al.*, 2009] and Paleozoic granites of >320 Ma in Southwest Tianshan [*Gao et al.*, 2009; *Gou et al.*, 2012; *Long et al.*, 2011; *Xu et al.*, 2013] are shown for comparison.

clinopyroxene fractionation. The model calculation suggests that ~30–40% ilmenite fractionation can produce low [Nb/La]$_{PM}$ and [Nb/Zr]$_{PM}$ values similar to the Haladala gabbro samples (Figure 8). However, large amounts (~30–40%) of ilmenite fractionation are unreasonable, suggesting that the extremely low [Nb/La]$_{PM}$ and Nb/Ta ratios must be partially inherited from a mantle source in addition to the effects by crustal contamination and ilmenite fractionation.

The Haladala gabbro samples show extremely variable Ti anomalies despite of their depletions of Nb and Ta (Figure 6 b). This can be attributed to the crystallization/accumulation of Fe-Ti oxides within the rocks as shown by the rough positive correlation between Ti/Ti* values and the proportion of Fe-Ti oxides (Figure S3). In addition, [Nb/La]$_{PM}$ and Nb/Ta ratios are also positively correlated with the proportion of Fe-Ti oxides, except for the two olivine-bearing samples (TKS1148 and TKS1156; Figure S3). This demonstrates that the crystallization/accumulation of Fe-Ti oxides, especially ilmenite, also accounts for the variation of [Nb/La]$_{PM}$ and Nb/Ta ratios. Samples TKS1148 and TKS1156 have slightly higher [Nb/La]$_{PM}$ and Nb/Ta ratios (Figure S3), probably owing to relatively higher proportion of ilmenite than Ti magnetite in the samples since that ilmenite has near chondritic Nb/Ta ratios but much higher Nb and Ta concentrations than Ti magnetite (Table S7). The Fe-Ti oxides in samples TKS1148 and TKS1156 would mostly be ilmenite as they are dendritic and interstitial to oli-

vine or plagioclase. The two samples have higher TiO$_2$ in comparison with other samples that contain similar proportions of Fe-Ti oxides (Tables S1 and S4).

5.3.3. A Hybrid Mantle Source

The Haladala gabbros have high zircon $\varepsilon_{Hf}(t)$, consistent with depleted bulk rock $\varepsilon_{Hf}(t)$ and $\varepsilon_{Nd}(t)$ values and low initial $^{87}Sr/^{86}Sr$ ratios. These isotopic signatures can be taken as evidence for an asthenosphere mantle source for the Haladala gabbros. The mantle beneath the orogenic zone is likely to consist of a complicated mixture of components formed by previous oceanic subduction followed by orogen formation and collapse processes. This suggests that the mantle source may have been hybridized by recycled crustal materials, as indicated by the high zircon $\delta^{18}O$ values of the Haladala gabbros ($\delta^{18}O = 5.69$–6.64‰; Table S3) and slightly decoupled Nd-Hf isotope (Figure 7b). The combination of subducted sediment (namely GLOSS) and recycled oceanic slab is compositionally similar to the upper continental crust (UCC) [*Plank and Langmuir*, 1998]. A recent hybridization involving GLOSS (or UCC), however, would not only contribute a Nb-Ta depletion, less radiogenic Sr-Nd-Hf isotopes, and high $\delta^{18}O$ values to the mantle source [*Roberts et al.*, 2013;

Plank and Langmuir, 1993] but also result in high potassium in the source, which contradicts with the composition of the Haladala gabbros. The good correlation between Nd and Hf isotopes of the Haladala gabbros is not oblique, but parallel to the mantle array line (Figure 7b), further arguing against the involvement of significant sediments in the mantle source. Accordingly, the recycled lower crust through orogeny collapse would be a more appropriate alternative for the geochemical and isotopic characteristics of the Haladala gabbros, based on its relatively low potassium contents in comparison to the upper crust [*Rudnick and Gao*, 2003].

The Haladala gabbros have higher $^{206}Pb/^{204}Pb$ ratios than the ~290 Ma mafic magmas of the Tarim LIP (Figures 7c and 7d) despite their U/Pb ratios (0.01–0.16; Table S4) lower than the latter (U/Pb = 0.10–0.37) [*Tian et al.*, 2010]. This reflects higher $^{206}Pb/^{204}Pb$ ratios of the mantle source of the Haladala gabbros relative to that of the Tarim Permian mafic rocks. The Haladala gabbros and Tarim Permian mafic rocks define a common trend on a $^{207}Pb/^{204}Pb$-$^{206}Pb/^{204}Pb$ diagram (Figure 7c), but the Haladala gabbros lie closer to the NHRL on the $^{208}Pb/^{204}Pb$-$^{206}Pb/^{204}Pb$ diagram (Figure 7d), which is also indicative of distinctive mantle sources. The ~290 Ma Tarim magmatism was derived from decompression melting of the mantle plume when interacted with the margins of old cratonic lithosphere, while the ~280 Ma event involved less lithosphere-plume interaction [*Wei et al.*, 2014; *Xu et al.*, 2014]. In contrast, the Haladala gabbros are the product of depleted mantle and minor interaction with juvenile orogenic lithosphere, given the widespread juvenile crust in CAOB [e.g., *Jahn et al.*, 2000; *Jahn*, 2004]. The integrated mantle source of the Haladala gabbros is much younger than that of the Tarim Permian mafic rocks according to their Nd-Hf isotopes (Figure 7b). Thus, the mantle source of the Haladala gabbros may have been recently refertilized by recycled crustal materials through processes such as South Tianshan oceanic subduction, orogeny, and consequent orogenic collapse during the Late Paleozoic [*Gao et al.*, 2011; *Han et al.*, 2011].

5.4. Subduction, Postorogenic Collapse, Slab Break-Off, or Mantle Plume

The Haladala gabbroic intrusion testifies to a significant mantle melting event. In general, mantle melting can be induced by heating, decompression, or volatile addition [e.g., *Farmer*, 2003; *Niu*, 2005]. Identification of the factors triggering mantle melting to generate the Haladala intrusion has important implications for the tectonic setting under which the magmas were generated.

The occurrence of the Haladala gabbroic intrusion in the Southwest Tianshan orogenic belt raises a possible subduction scenario for its generation. Subduction process has also been considered to account for the generation of intraplate mafic volcanism, even for some classic "plume" flood basalt province such as Columbia River [*Stefano et al.*, 2011; *Cabato et al.*, 2015] and Siberian Traps [*Ivanov et al.*, 2008; *Ivanov and Litasov*, 2013]. Within this scheme, addition of volatiles released from the dehydration of subducted oceanic slab may be the key factor to induce mantle melting [e.g., *Cabato et al.*, 2015; *Faccenda*, 2014; *Ivanov*, 2015]. Alaskan-type ultramafic intrusions, typical products of island arcs [e.g., *Irvine*, 1974; *Ishiwatari and Ichiyama*, 2004], are generally unlayered but display distinctive cumulate textures. They exhibit a concentric architecture that consists of successive lithofacies including dunite, wehrlite, olivine clinopyroxenite, hornblende clinopyroxenite, hornblendite, and hornblende gabbro from core to rim [*Irvine*, 1974], suggesting a hydrous magma composition. This model is clearly not applicable to the Haladala gabbros because (a) the lack of hydrous minerals (biotite or hornblende) is very different from mafic intrusions related to fluid metasomatism [e.g., *Väisänen et al.*, 2000; *Huang et al.*, 2012] or subduction [e.g., *Claeson and Meurer*, 2004; *Ivanov*, 2015]; (b) the early mineral assemblage of troctolite (Figure 3c) in a mafic cumulate sequence points to an anhydrous (water poor) parental magma [*Gaetani et al.*, 1993; *Niu*, 2005]; (c) occurrence of magnetite layers in the upper section of the Haladala intrusion [*Gao et al.*, 1991] indicates extensive fractional crystallization of an anhydrous primary magma under reduced environment; (d) the emplacement of the Haladala gabbros (~300 Ma) postdated slab subduction of the South Tianshan Ocean, which most likely terminated before ~ 320 Ma [e.g., *Gao et al.*, 2011; *Han et al.*, 2011].

The emplacement of the Haladala gabbros likely took place in a postcollisional setting. In this scenario, decompression melting in an orogenic belt is mainly induced by gravitational collapse of thickened crust. The geochemical and isotopic characteristics of the Haladala gabbros require the involvement of recycled lower crust in their magma source. Nevertheless, the Haladala gabbros are distinct from the postcollisional magmatism that is typically characterized by medium-K to high-K calc-alkaline to shoshonitic to ultrapotassic igneous suites [e.g., *Bonin*, 2004; *Huang et al.*, 2010].

Alternatively, anomaly-related heating is a potential major mechanism for producing the Haladala gabbros. Asthenosphere mantle diapirs due to slab break-off (e.g., subduction of Tianshan oceanic slab) or a mantle plume (e.g., Tarim mantle plume) are the two most plausible anomalies for heating of the lithospheric mantle in the studied area. Since the Haladala gabbros were emplaced after the collision period, a mantle plume is the most feasible for this scenario. Supporting evidence for this argument can be found from the main geochemical and petrological features of the Haladala gabbros.

1. The Haladala gabbros are characterized by their overall alkali-rich contents. However, they are sodic and depleted in K, suggesting a predominantly asthenospheric source with only a minor proportion of recycled crustal materials. Lack of hydrous minerals and presence of troctolite in the layered intrusion indicate an essentially dry source.
2. Presence of thick V-Ti magnetite-rich layers (>1 m) in the upper part of the Haladala intrusion (Figures 2b and 2c) demonstrates extensive fractionation in large magmatic systems. The latter is typical of plume-generated LIPs, such as the Panzhihua mafic complex of the Permian Emeishan LIP in Southwest China [e.g., *Zhou et al.*, 2005] and the Bushveld complex of the Palaeoproterozoic Bushveld LIP in South Africa [e.g., *Harney and von Gruenewaldt*, 1995; *Godel et al.*, 2011].

It is interesting to note that the emplacement of the Haladala gabbros is coeval with the Wajilitag diamondiferous kimberlites [*Zhang et al.*, 2013]. The diamondiferous kimberlites and kimberlite-flood basalt association in the Tarim LIP are similar to those observed in other LIPs [e.g., *Gibson et al.*, 1995; *Heaman and Kjarsgaard*, 2000; *Chalapathi-Rao and Lehmann*, 2011] and have tentatively been attributed to mantle plumes [*Xu et al.*, 2014]. Interestingly, the Wajilitag kimberlites erupted ~10 Ma earlier than the flood basalts, likely marking the onset of plume-induced magmatism in Tarim [*Zhang et al.*, 2013; *Xu et al.*, 2014]. Permian basic volcanic rocks are widely distributed in the western part of northern Tarim uplift and northern Tarim depression [*Tian et al.*, 2010; *Yu et al.*, 2011; *Wei et al.*, 2014; *Xu et al.*, 2014]. Plume-related Permian magmatism also extended to the Junggar and Tuha Basins and Altay Orogen [*Zhang et al.*, 2010b; *Qin et al.*, 2011]. It is therefore possible that the Tarim mantle plume also affected the western Tianshan, and the Haladala gabbroic intrusion likely represents the early melting products of the Tarim mantle plume.

5.5. Preferential Emplacement of Plume-Derived Melts Along Lithospheric Weak Zones

The lithosphere beneath the Tarim craton is relatively thick and greater than 140 km at present [*Liu et al.*, 2004; *Priestley et al.*, 2006]. It may have been even thicker in the Permian [*Wei et al.*, 2014; *Xu et al.*, 2014]. The thick cratonic keel is generally resistant to pervasive modification by hot spot processes [*Sleep et al.*, 2002; *Burov et al.*, 2007; *Villemaire et al.*, 2012]. In addition, a thick lithosphere (>130 km) will hamper the upwelling of a mantle plume, thus preventing its decompression melting [*Davies*, 1994; *Sleep et al.*, 2002; *Jourdan et al.*, 2007; *Foley*, 2008]. In contrast, the lithosphere of a young orogen may suffer pervasive modification during the magmatism that results from heating by a mantle plume [*Villemaire et al.*, 2012]. The modification involves plume materials ascending to the surface or ponding at the base of the lithosphere [e.g., *Sleep et al.*, 2002], as well as heating and partial melting of the lower crust and lithospheric mantle [e.g., *Saleeby et al.*, 2003]. All these processes would induce orogenic collapse and production of juvenile crust [*Murphy et al.*, 1998; *Betts et al.*, 2009]. The orogenic belt represents weakened lithospheric zones that are preferred zones of emplacement for plume-, lithospheric mantle-, and lower crust-derived magmas [*Murphy et al.*, 1998; *Betts et al.*, 2009]. The preferential emplacement of mantle-derived magmas along an orogenic belt is further assisted by its postcollisional extension tectonics.

In the Tarim case, the thick cratonic keel might deflect the mantle flow, which then ponded plume material beneath the local regions of thinner lithosphere [*Sleep*, 1997; *Sleep et al.*, 2002; *Burov et al.*, 2007] or in the low-stress regions associated with rifting structures [e.g., *Petit and Ebinger*, 2000]. The Western Tianshan orogenic belt to the north of the Tarim Craton is such a region where the Tarim mantle plume would have preferred to flow. The preexisting mantle beneath the Western Tianshan orogenic belt may have been hybridized by subducted oceanic crust and then refertilized by lower crust due to orogenic collapse. The refertilized mantle beneath the young orogenic belt had a lower solidus temperature than the normal mantle; and thus, mantle melting took place as a result of thermal perturbation by the ponding of plume materials. In addition, the preferential partial melting of refertilized mantle would also dilute the geochemical features of melts derived from decompression melting of the plume.
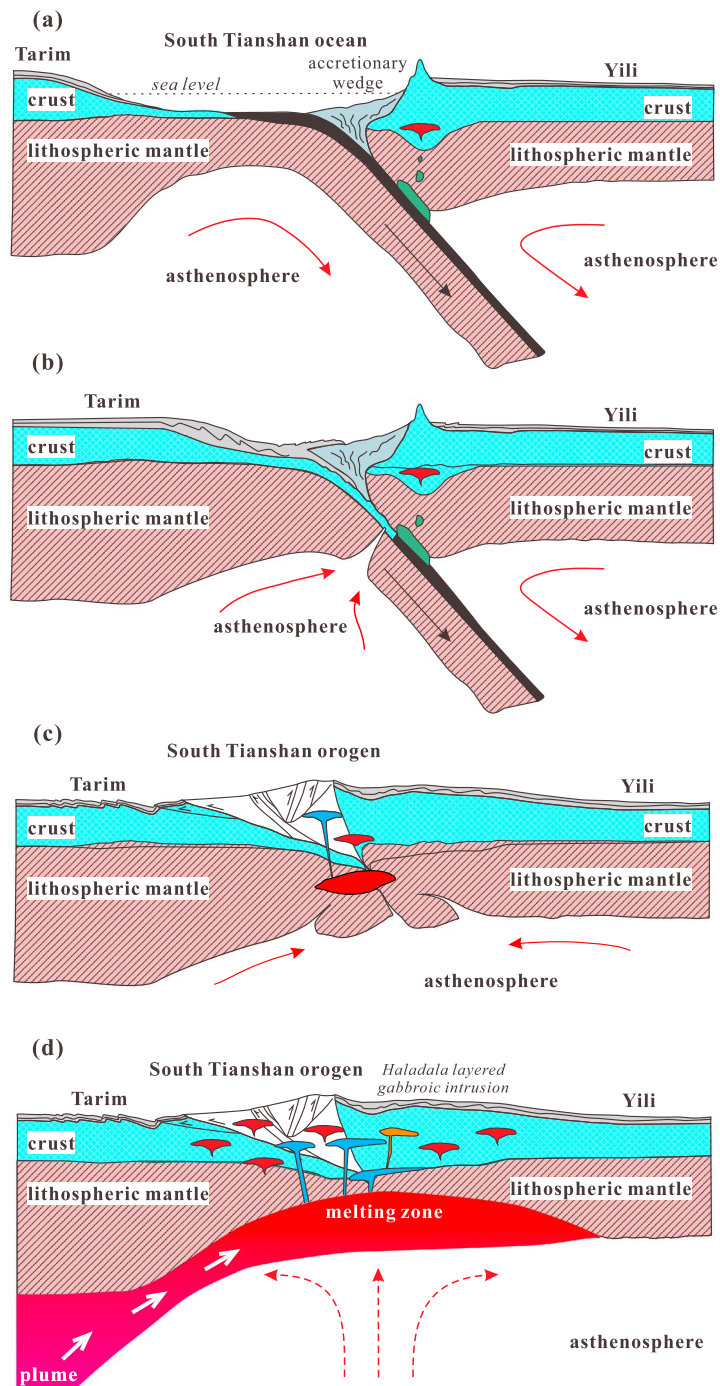
Figure 9. Schematic illustration of the suggested model for the petrogenesis and evolution of the Haladala layered gabbroic intrusion. (a) South Tianshan oceanic crust subducted northward beneath the Yili Block, dehydrated, and produced arc magmas. (b) The Tarim Craton collided with the Yili Block, and the denser oceanic lithosphere was detached from the buoyant continental lithosphere. (c) Asthenospheric mantle replaced the space vacated by the slab break-off and subsequent orogenic collapse beneath the South Tianshan Orogen. Upwelling asthenospheric mantle underwent partial melting and triggered postcollisional high-K calc-alkaline to ultrapotassic magmatisms. (d) The hot mantle plume material ponded preferentially beneath the Tianshan orogenic belt probably due to deflection by the thick Tarim craton, which accelerated orogenic collapse and allowed further storage of plume material at the base of preexisting lithospheric weak zone. Mantle plume material, mixing with minor lithospheric mantle refertilized by recycled lower crust and recycled oceanic slab, underwent partial melting and generated widespread magmatism including the Haladala layered gabbroic intrusion in the Tianshan orogenic belt.

In the early Carboniferous, the South Tianshan Ocean was subducted northward beneath the Yili Block (Figure 9a). The dehydration of subducted oceanic crust triggered the partial melting of mantle wedge and the continental crust to produce arc magmas [e.g., *Gao et al.*, 2009]. The Tarim Craton collided with the Yili Block at ~ 320 Ma when the South Tianshan Ocean was extinct (Figure 9b) [e.g., *Gao et al.*, 2011; *Han et al.*, 2011], and subsequent break-off of the oceanic crust might have uplifted the orogen, steepened the sutures, backpropagated the thrusts within the orogen, and triggered postcollisional high-K calc-alkaline to ultrapotassic magmatisms (Figure 9c) [e.g., *Gou et al.*, 2012]. At about 300 Ma, the Western Tianshan orogenic belt, as a lithospheric weak zone, became the favorable site to accommodate deflected flow of the Tarim mantle plume (Figure 9d). This resulted in the formation of the Haladala gabbros.

6. Conclusions

The Haladala layered gabbroic intrusion was formed at the end of Carboniferous (~ 300 Ma). The rocks have strongly positive bulk rock $\varepsilon_{Nd}(t)$ and $\varepsilon_{Hf}(t)$, low initial $^{87}Sr/^{86}Sr$ and DUPAL-like Pb isotopic ratios, strong positive zircon $\varepsilon_{Hf}(t)$, and overall high $\delta^{18}O$, as well as negative Ta and Nb and notable positive Sr and Pb anomalies.

The lack of hydrous minerals and low K contents distinguish the Haladala gabbros from arc or postcollisional magmatism. The low oxygen fugacity, which is required for the gradual enrichment of V-Ti magnetite during the magma fractionation, and troctolite mineral assemblage (olivine + plagioclase) suggest an essentially dry mantle source.

The Haladala gabbros, as well as the Wajilitag kimberlites [*Zhang et al.*, 2013], are interpreted as the earliest magmatism (~300 Ma) of the Tarim mantle plume. Its occurrence in the Tianshan Orogenic belt is due to the preferential flow of the Tarim mantle plume along lithospheric weak zones.

References

Allen, M. B., B. F. Windley, and C. Zhang (1992), Palaeozoic collisional tectonics and magmatism of the Chinese Tien Shan, central Asia, *Tectonophysics*, 220, 89–115, doi:10.1016/0040-1951(93)90225-9.

Aulbach, S., S. Y. O'Reilly, W. L. Griffin, and N. J. Pearson (2008), Subcontinental lithospheric mantle origin of high niobium/tantalum ratios in eclogites, *Nat. Geosci.*, 1, 468–472, doi:10.1038/ngeo226.

Baker, J., and T. Waight (2002), Pb isotope analysis using Tl and a ^{207}Pb-204Pb spike on a double focusing MC-ICPMS, *Geochim. Cosmochim. Acta*, 66, A44.

Barnes, C. G., G. Dumond, A. S. Yoshinobu, and T. Prestvik (2004), Assimilation and crystal accumulation in a mid-crustal magma chamber: The Sausfjellet pluton, north-central Norway, *Lithos*, 75, 389–412, doi:10.1016/j.lithos.2004.04.036.

Barth, M. G., W. F. McDonough, and R. L. Rudnick (2000), Tracking the budget of Nb and Ta in the continental crust, *Chem. Geol.*, 165, 197–213, doi:10.1016/S0009-2541(99)00173-4.

Bazhenov, M. L., A. Q. Collins, K. E. Degtyarev, N. M. Levashova, A. V. Mikolaichuk, V. E. Pavlov, and R. V. Voo (2003), Paleozoic northward drift of the North Tien Shan (Central Asia) as revealed by Ordovician and Carboniferous paleomagnetism, *Tectonophysics*, 366, 113–141, doi:10.1016/S0040-1951(03)00075-1.

Beard, J. S. (1986), Characteristic mineralogy of arc-related cumulate gabbros: Implications for the tectonic setting of gabbroic plutons and for andesite genesis, *Geology*, 14, 848–851, doi:10.1130/0091-7613(1986)14<848:CMOACG>2.0.CO;2.

Bédard, J. H. (2001), Parental magmas of the Nain Plutonic Suite anorthosites and mafic cumulates: A trace element modelling approach, *Contrib. Mineral. Petrol.*, 141, 747–771.

Betts, P. G., D. Giles, J. Foden, B. F. Schaefer, G. Mark, M. J. Pankhurst, C. J. Forbes, H. A. Williams, N. C. Chalmers, and Q. Hills (2009), Mesoproterozoic plume-modified orogenesis in eastern Precambrian Australia, *Tectonics*, 28, TC3006, doi:10.1029/2008TC002325.

Bonin, B. (2004), Do coeval mafic and felsic magmas in post-collisional to within-plate regimes necessarily imply two contrasting, mantle and crustal, sources? A review, *Lithos*, 78, 1–24, doi:10.1016/j.lithos.2004.04.042.

Bowles, J. F. W., H. M. Prichard, S. Suarez, and P. C. Fisher (2013), The first report of platinum-group minerals in magnetite-bearing gabbro, Freetown layered complex, Sierra Leone: Occurrences and genesis, *Can. Mineral.*, 51, 455–473, doi:10.3749/canmin.51.3.455.

Brooks, C. K., R. R. Keays, D. D. Lambert, L. R. Frick, and T. F. D. Nielsen (1999), Re-Os isotope geochemistry of Tertiary picritic and basaltic magmatism of East Greenland: Constraints on plume-lithosphere interactions and the genesis of the Platinova reef, Skaergaard intrusion, *Lithos*, 47, 107–126, doi:10.1016/S0024-4937(99)00010-9.

Burov, E., L. Guillou-Frottier, E. d'Acremont, L. Le Pourhiet, and S. Cloetingh (2007), Plume head–lithosphere interactions near intra-continental plate boundaries, *Tectonophysics*, 434, 15–38, doi:10.1016/j.tecto.2007.01.002.

Cabato, J. A., C. J. Stefano, and S. B. Mukasa (2015), Volatile concentrations in olivine-hosted melt inclusions from the Columbia River flood basalts and associated lavas of the Oregon Plateau: Implications for magma genesis, *Chem. Geol.*, 392, 59–73, doi:10.1016/j.chemgeo.2014.11.015.

Campbell, I. H. (2007), Testing the plume theory, *Chem. Geol.*, 241, 153–176.

Campbell, I. H., and R. W. Griffiths (1990), Implications of mantle plume structure for the evolution of flood basalts, *Earth Planet. Sci. Lett.*, 99, 79–93.

Cao, J., C. Y. Wang, C. M. Xing, and Y. G. Xu (2014), Origin of the early Permian Wajilitag igneous complex and associated Fe-Ti oxide mineralization in the Tarim large igneous province, NW China, *J. Asian Earth Sci.*, 84, 51–68, doi:10.1016/j.jseaes.2013.09.014.

Castillo, P. (1988), The Dupal anomaly as a trace of the upwelling lower mantle, *Nature*, 336, 667–670, doi:10.1038/336667a0.

Cawthorn, R. G., and L. D. Ashwal (2009), Origin of anorthosite and magnetite layers in the Bushveld complex, constrained by major element compositions of plagioclase, *J. Petrol.*, 50, 1607–1637, doi:10.1093/petrology/egp042.

Chalapathi-Rao, N. V., and B. Lehmann (2011), Kimberlites, flood basalts and mantle plumes: New insights from the Deccan large igneous province, *Earth Sci. Rev.*, 107, 315–324, doi:10.1016/j.earscirev.2011.04.003.

Chauvel, C., E. Lewin, M. Carpentier, N. T. Arndt, and J. C. Marini (2008), Role of recycled oceanic basalt and sediment in generating the Hf-Nd mantle array, *Nat. Geosci.*, *1*, 64–67, doi:10.1038/ngeo.2007.51.

Christensen, N. I., and J. D. Smewing (1981), Geology and seismic structure of the northern section of the Oman ophiolite, *J. Geophys. Res.*, *86*, 2545–2555, doi:10.1029/JB086iB04p02545.

Claeson, D. T., and W. P. Meurer (2004), Fractional crystallization of hydrous basaltic 'arc-type' magmas and the formation of amphibole-bearing gabbroic cumulates, *Contrib. Mineral. Petrol.*, *147*, 288–304, doi:10.1007/s00410-003-0536-0.

Courtillot, V., A. Davaille, J. Besse, and J. Stock (2003), Three distinct types of hotspots in the Earth's mantle, *Earth Planet. Sci. Lett.*, *205*, 295–308.

Davies, G. F. (1994), Thermomechanical erosion of the lithosphere by mantle plumes, *J. Geophys. Res.*, *99*, 15,709–15,722, doi:10.1029/94JB00119.

Donnelly, K. E., S. L. Goldstein, C. H. Langmuir, and M. Spiegelman (2004), Origin of enriched ocean ridge basalts and implications for mantle dynamics, *Earth Planet. Sci. Lett.*, *226*, 347–366, doi:10.1016/j.epsl.2004.07.019.

Dygert, N., Y. Liang, and P. Hess (2013), The importance of melt TiO_2 in affecting major and trace element partitioning between Fe-Ti oxides and lunar picritic glass melts, *Geochim. Cosmochim. Acta*, *106*, 134–151, doi:10.1016/j.gca.2012.12.005.

Ellam, R. M., R. W. Carlson, and S. B. Shirey (1992), Evidence from Re-Os isotopes for plume-lithosphere mixing in Karoo flood basalt genesis, *Nature*, *359*, 718–721, doi:10.1038/359718a0.

Faccenda, M. (2014), Water in the slab: A trilogy, *Tectonophysics*, *614*, 1–30, doi:10.1016/j.tecto.2013.12.020.

Farmer, G. L. (2003), Continental basaltic rocks, in *Treatise on Geochemistry*, vol. 3, edited by R. L. Rudnick, pp. 85–121, Elsevier-Pergamon, Oxford.

Foley, S. F. (2008), Rejuvenation and erosion of the cratonic lithosphere, *Nat. Geosci.*, *1*, 503–510, doi:10.1038/ngeo261.

Gaetani, G. A., T. L. Grove, and W. B. Bryan (1993), The influence of water on the petrogenesis of subduction-related igneous rocks, *Nature*, *365*, 332–334, doi:10.1038/365332a0.

Gallagher, K., and C. Hawkesworth (1992), Dehydration melting and the generation of continental flood basalts, *Nature*, *358*, 57–59, doi:10.1038/358057a0.

Gao, J. P., X. Z. Li, H. Q. Yang, Y. P. Luo, and W. G. Yao (1991), A study on the geological characteristics and ore finding prospects of Tekesi basic body in Xinjiang [in Chinese English abstract], *Northwest Geosci.*, *3*, 131–143.

Gao, J., M. S. Li, X. C. Xiao, Y. Tang, and G. Q. He (1998), Paleozoic tectonic evolution of the Tianshan Orogen, northwestern China, *Tectonophysics*, *287*, 213–231, doi:10.1016/S0040-1951(97)00211-4.

Gao, J., L. L. Long, R. Klemd, Q. Qian, D. Y. Liu, X. M. Xiong, W. Su, W. Liu, Y. T. Wang, and F. Q. Yang (2009), Tectonic evolution of the South Tianshan Orogen and adjacent regions, NW China: Geochemical and age constraints of granitic rocks, *Int. J. Earth Sci. (Geol. Rundsch.)*, *98*, 1221–1238, doi:10.1007/s00531-008-0370-8.

Gao, J., R. Klemd, Q. Qian, X. Zhang, J. L. Li, T. Jiang, and Y. Q. Yang (2011), The collision between the Yili and Tarim blocks of the Southwestern Altaids: Geochemical and age constraints of a leucogranite dike crosscutting the HP-LT metamorphic belt in the Chinese Tianshan Orogen, *Tectonophysics*, *499*, 118–131, doi:10.1016/j.tecto.2011.01.001.

Ge, S. S., M. G. Zhai, I. Safonova, D. P. Li, X. Y. Zhu, P. F. Zou, and H. X. Shan (2015), Whole-rock geochemistry and Sr-Nd-Pb isotope systematics of the Late Carboniferous volcanic rocks of the Awulale metallogenic belt in the western Tianshan Mountains (NW China): Petrogenesis and geodynamical implications, *Lithos*, *228*, 62–77, doi:10.1016/j.lithos.2015.04.019.

Gibson, S. A., R. N. Thompson, A. P. Dickin, and O. H. Leonardos (1995), High-Ti and low-Ti mafic potassic magmas: Key to plume-lithosphere interactions and continental flood-basalt genesis, *Earth Planet. Sci. Lett.*, *136*, 149–165, doi:10.1016/0012-821X(95)00179-G.

Godel, B., S. J. Barnes, and W. D. Maier (2011), Parental magma composition inferred from trace element in cumulus and intercumulus silicate minerals: An example from the Lower and Lower Critical zones of the Bushveld complex, South Africa, *Lithos*, *125*, 537–552, doi:10.1016/j.lithos.2011.03.010.

Gou, L. L., L. F. Zhang, R. B. Tao, and J. X. Du (2012), A geochemical study of syn-subduction and post-collisional granitoids at Muzhaerte River in the Southwest Tianshan UHP belt, NW China, *Lithos*, *136*, 201–224, doi:10.1016/j.lithos.2011.10.005.

Green, T. H., and N. J. Pearson (1987), An experimental study of Nb and Ta partitioning between Ti-rich minerals and silicate liquids at high pressure and temperature, *Geochim. Cosmochim. Acta*, *51*, 55–62, doi:10.1016/0016-7037(87)90006-8.

Han, B. F., G. Q. He, X. C. Wang, and Z. J. Guo (2011), Late Carboniferous collision between the Tarim and Kazakhstan-Yili terranes in the western segment of the South Tian Shan Orogen, Central Asia, and implications for the Northern Xinjiang, western China, *Earth Sci. Rev.*, *109*, 74–93, doi:10.1016/j.earscirev.2011.09.001.

Harney, D. M. W., and G. von Gruenewaldt (1995), Ore-forming processes in the upper part of the Bushveld complex, South Africa, *J. Afr. Earth Sci.*, *20*, 77–89, doi:10.1016/0899-5362(95)00034-Q.

Hart, S. R. (1984), A large-scale isotope anomaly in the Southern Hemisphere mantle, *Nature*, *309*, 753–757, doi:10.1038/309753a0.

Hawkesworth, C. J., M. S. M. Mantovani, P. N. Taylor, and Z. Palacz (1986), Evidence from the Parana of south Brazil for a continental contribution to Dupal basalts, *Nature*, *322*, 356–359, doi:10.1038/322356a0.

Hawkesworth, C. J., K. Gallagher, J. M. Hergt, and F. McDermott (1993), Mantle and slab contributions in arc magmas, *Annu. Rev. Earth Planet. Sci.*, *21*, 175–204, doi:10.1146/annurev.earth.21.1.175.

He, P. L., X. L. Huang, H. Y. Li, J. Li, Y. Yu, and W. X. Li (2013), Mechanism of Fe-Ti enrichment in the Haladala gabbros: Implication for the tectonic evolution of the western Tianshan orogenic belt [in Chinese English abstract], *Acta Petrol. Sin.*, *29*, 3457–3472.

Heaman, L. M., and B. A. Kjarsgaard (2000), Timing of eastern North American kimberlite magmatism: Continental extension of the Great Meteor hotspot track?, *Earth Planet. Sci. Lett.*, *178*, 253–268, doi:10.1016/S0012-821X(00)00079-0.

Huang, T. K., J. S. Ren, C. F. Jiang, Z. M. Zhang, and D. Y. Qian (1987), *Geotectonic Evolution of China*, 203 pp., Springer, New York.

Huang, X. L., Y. L. Niu, Y. G. Xu, L. L. Chen, and Q. J. Yang (2010), Mineralogical and geochemical constraints on the petrogenesis of post-collisional potassic and ultrapotassic rocks from western Yunnan, SW China, *J. Petrol.*, *51*, 1617–1654, doi:10.1093/petrology/egq032.

Huang, X. L., J. W. Zhong, and Y. G. Xu (2012), Two tales of the continental lithospheric mantle prior to the destruction of the North China Craton: Insights from Early Cretaceous mafic intrusions in western Shandong, East China, *Geochim. Cosmochim. Acta*, *96*, 193–214, doi:10.1016/j.gca.2012.08.014.

Huang, X. L., Y. L. Niu, Y. G. Xu, J. L. Ma, H. N. Qiu, and J. W. Zhong (2013), Geochronology and geochemistry of Cenozoic basalts from eastern Guangdong, SE China: Constraints on the lithosphere evolution beneath the northern margin of the South China Sea, *Contrib. Mineral. Petrol.*, *165*, 437–455, doi:10.1007/s00410-012-0816-7.

Iizuka, T., and T. Hirata (2005), Improvements of precision and accuracy in in-situ Hf isotope microanalysis of zircon using the laser ablation-MC-ICPMS technique, *Chem. Geol.*, *220*, 121–137, doi:10.1016/j.chemgeo.2005.03.010.

Ionov, D. A., and A. W. Hofmann (1995), Nb–Ta-rich mantle amphiboles and micas: Implications for subduction-related metasomatic trace element fractionations, *Earth Planet. Sci. Lett.*, *131*, 341–356, doi:10.1016/0012-821X(95)00037-D.

Irvine, T. N. (1974), Petrology of the Duke Island ultramafic complex southern Alaska, *Geol. Soc. Am. Mem.*, *138*, 1–244.

Ishiwatari, A., and Y. Ichiyama (2004), Alaskan-type plutons and ultramafic lavas in Far East Russia, Northeast China, and Japan, *Int. Geol. Rev.*, *46*, 316–331, doi:10.2747/0020-6814.46.4.316.

Ivanov, A. V. (2015), Why volatiles are required for cratonic flood basalt volcanism: Two examples from the Siberian Craton, in *The Interdisciplinary Earth: A Volume in Honor of Don L. Anderson*, *Geol. Soc. Am. Spec. Pap.*, vol. 514, edited by G. R. Foulger, M. Lustrino, and S. D. King, pp. 325–338, AGU, Washington, D. C., doi:10.1130/2015.2514(19).

Ivanov, A. V., and K. D. Litasov (2013), The deep water cycle and flood basalt volcanism, *Int. Geol. Rev.*, *56*, 1–14, doi:10.1080/00206814.2013.817567.

Ivanov, A. V., E. I. Demonterova, S. V. Rasskazov, and T. A. Yasnygina (2008), Low-Ti melts from the Southeastern Siberian Traps Large Igneous Province: Evidence for a water-rich mantle source?, *J. Earth Syst. Sci.*, *117*, 1–21.

Jahn, B. M. (2004), The Central Asian Orogenic Belt and growth of the continental crust in the Phanerozoic, *Geol. Soc., London, Spec. Publ.*, *226*, 73–100, doi:10.1144/GSL.SP.2004.226.01.05.

Jahn, B. M., F. Y. Wu, and B. Chen (2000), Granitoids of the Central Asian Orogenic Belt and continental growth in the Phanerozoic, *Trans. R. Soc. Edinburgh: Earth Sci.*, *91*, 181–193.

Jiang, C. Y., C. Z. Jia, L. C. Li, P. B. Zhang, D. R. Lu, and K. Y. Bai (2004), Source of the Fe-riched-type high-Mg magma in Mazhartag region, Xinjiang [in Chinese with English abstract], *Acta Geol. Sin.*, *78*, 770–780.

Jiang, C. Y., Y. Z. Li, P. B. Zhang, and S. F. Ye (2006), Petrogenesis of Permian basalts on the western margin of the Tarim basin, China, *Russ. Geol. Geophys.*, *47*, 237–248.

Jourdan, F., G. Féraud, H. Bertrand, and M. K. Watkeys (2007), From flood basalts to the inception of oceanization: Example from the ^{40}Ar/^{39}Ar high-resolution picture of the Karoo large igneous province, *Geochem. Geophys. Geosyst.*, *8*, Q02002, doi:10.1029/2006GC001392.

Kelemen, P. B., N. Shimizu, and T. Dunn (1993), Relative depletion of niobium in some arc magmas and the continental crust: Partitioning of K, Nb, La and Ce during melt/rock reaction in the upper mantle, *Earth Planet. Sci. Lett.*, *120*, 111–134, doi:10.1016/0012-821X(93)90234-Z.

Klemme, S., D. Gunther, K. Hametner, S. Prowatke, and T. Zack (2006), The partitioning of trace elements between ilmenite, ulvospinel, armalcolite and silicate melts with implications for the early differentiation of the moon, *Chem. Geol.*, *234*, 251–263, doi:10.1016/j.chemgeo.2006.05.005.

Li, C. S., Y. Tao, L. Qi, and E. M. Ripley (2012a), Controls on PGE fractionation in the Emeishan picrites and basalts: Constraints from integrated lithophile-siderophile elements and Sr-Nd isotopes, *Geochim. Cosmochim. Acta*, *90*, 12–32, doi:10.1016/j.gca.2012.04.046.

Li, H. Y., X. L. Huang, W. X. Li, J. Cao, P. L. He, and Y. G. Xu (2014), Age and geochemistry of the Early Permian basalts from Qimugan in the southwestern Tarim basin [in Chinese with English abstract], *Acta Petrol. Sin.*, *29*, 3353–3368.

Li, J. L., Q. Qian, J. Gao, W. Su, X. Zhang, X. Liu, and T. Jiang (2010a), Geochemistry, zircon U-Pb ages and tectonic settings of the Dahalajunshan volcanics and granitic intrusions form the Adengtao area in the Southeast Zhaosu, western Tianshan Mountains [in Chinese with English abstract], *Acta Petrol. Sin.*, *26*, 2913–2924.

Li, X. H., W. X. Li, Q. L. Li, X. C. Wang, Y. Liu, and Y. H. Yang (2010b), Petrogenesis and tectonic significance of the 850 Ma Gangbian alkaline complex in South China: Evidence from in situ zircon U–Pb dating, Hf-O isotopes and whole-rock geochemistry, *Lithos*, *114*, 1–15, doi:10.1016/j.lithos.2009.07.011.

Li, X. H., et al. (2010c), Penglai zircon megacrysts: A potential new working reference material for microbeam determination of Hf-O isotopes and U–Pb age, *Geostand. Geoanal. Res.*, *34*, 117–134.

Li, X. H., G. Q. Tang, B. Gong, Y. H. Yang, K. J. Hou, Z. C. Hu, Q. L. Li, Y. Liu, and W. X. Li (2013), Qinghu zircon: A working reference for microbeam analysis of U-Pb age and Hf and O isotopes, *Chin. Sci. Bull.*, *58*, 4647–4654, doi:10.1007/s11434-013-5932-x.

Li, Y. Q., Z. L. Li, H. L. Chen, S. F. Yang, and X. Yu (2012b), Mineral characteristics and metallogenesis of the Wajilitag layered mafic-ultramafic intrusion and associated Fe-Ti-V oxide deposit in the Tarim large igneous province, northwest China, *J. Asian Earth Sci.*, *49*, 161–174, doi:10.1016/j.jseaes.2011.11.026.

Li, Z. L., Y. Q. Li, H. L. Chen, M. Santosh, S. F. Yang, Y. G. Xu, C. H. Langmuir, Z. X. Chen, X. Yu, and S. Y. Zou (2012c), Hf isotopic characteristics of the Tarim Permian large igneous province rocks of NW China: Implication for the magmatic source and evolution, *J. Asian Earth Sci.*, *49*, 191–202, doi:10.1016/j.jseaes.2011.11.021.

Liang, X. R., G. J. Wei, X. H. Li, and Y. Liu (2003), Precise measurement of ^{143}Nd/^{144}Nd and Sm/Nd ratios using multiple-collectors inductively couple plasma-mass spectrometer (MC-ICP-MS) [in Chinese with English abstract], *Geochimica*, *32*, 91–96.

Lin, J. F., and Y. H. Deng (1996), Characteristics of the magnetite veins in Haladala gabbro massif in Xinjiang and their geological significance [in Chinese with English abstract], *Miner. Resour. Geol.*, *10*, 165–171.

Liu, J., Y. J. Li, X. G. Wang, and W. J. Guo (2006), Geochemical characteristics and tectonic environment of the Yishijilike Formation volcanic rocks in the Awulale area of Western Tianshan [in Chinese with English abstract], *Xinjiang Geol.*, *24*, 105–108.

Liu, S. W., L. S. Wang, C. Li, H. Li, Y. B. Han, C. Z. Jia, and G. Q. Wei (2004), Thermal-rheological structure of lithosphere beneath the northern flank of Tarim Basin, western China: Implications for geodynamics, *Sci. China, Ser. D: Earth Sci.*, *47*, 659–672, doi:10.1360/03yd0471.

Liu, Y. S., Z. C. Hu, S. Gao, D. Gunther, J. Xu, C. G. Gao, and H. H. Chen (2008), In situ analysis of major and trace elements of anhydrous minerals by LA-ICP-MS without applying an internal standard, *Chem. Geol.*, *257*, 34–43, doi:10.1016/j.chemgeo.2008.08.004.

Long, L. L., J. Gao, R. Klemd, C. Beier, Q. Qian, X. Zhang, J. B. Wang, and T. Jiang (2011), Geochemical and geochronological studies of granitoid rocks from the Western Tianshan Orogen: Implications for continental growth in the southwestern Central Asian Orogenic Belt, *Lithos*, *126*, 321–340, doi:10.1016/j.lithos.2011.07.015.

Long, L. L., Y. W. Wang, P. Z. Tang, L. J. Wang, J. B. Wang, and Z. Liao (2012), A debate on the special circumstance of rock-forming and ore-forming of Haladala pluton, amafic-ultramafic complex related to CuNi-VTiFe composite mineralizaiong, in Western Tianshan [in Chinese English abstract], *Acta Petrol. Sin.*, *28*, 2015–2028.

Ludwig, K. R. (2003), *User's Manual for Isoplot 3.00. A Geochronological Toolkit for Microsoft Excel*, *Spec. Publ.*, vol. 4a, Berkeley Geochronology Center, Berkeley, Calif.

Luo, Y., H. C. Niu, Q. Shan, B. Zhang, C. P. Zhou, W. B. Yang, and X. Y. Yu (2009), Discovery of the basaltic andesite-high-K basaltic andesite-trachyandesite association in the Yuximolegai Daban, West Tianshan and its geological significance [in Chinese with English abstract], *Acta Petrol. Sin.*, *25*, 934–943.

Ma, R. S., C. Y. Wang, and S. F. Ye (1993), *Tectonic Framework and Crustal Evolutional of Eastern Tianshan Mountains* [in Chinese with English abstract], pp. 1–225, Publishing House of Nanjing Univ., Nanjing.

Mcbirney, A. R. (1995), Mechanisms of differentiation in the Skaergaard intrusion, *J. Geol. Soc.*, *152*, 421–435, doi:10.1144/gsjgs.152.3.0421.

Morgan, W. J. (1971), Convection plumes in the lower mantle, *Nature*, *230*, 42–43.

Murphy, J. B., G. L. Oppliger, G. H. Brimhall, and A. Hynes (1998), Plume-modified orogeny: An example from the western United States, *Geology*, *26*, 731–734.

Niu, Y. L. (2005), Generation and evolution of basaltic magmas: Some basic concepts and a new view on the origin of Mesozoic-Cenozoic basaltic volcanism in Eastern China, *Geol. J. China Univ. (Engl. Ed.)*, *11*, 9–46.

Peccerillo, A. (1985), Roman comagmatic province (Central Italy)—Evidence for subduction-related magma genesis, *Geology*, *13*, 103–106, doi:10.1130/0091-7613(1985)13<103:RCPCIE>2.0.CO;2.

Petit, C., and C. Ebinger (2000), Flexure and mechanical behavior of cratonic lithosphere: Gravity models of the East African and Baikal rifts, *J. Geophys. Res.*, *105*, 19,151–19,162, doi:10.1029/2000JB900101.

Pik, R., C. Deniel, C. Coulon, G. Yirgu, and B. Marty (1999), Isotopic and trace element signatures of Ethiopian flood basalts: Evidence for plume-lithosphere interactions, *Geochim. Cosmochim. Acta*, *63*, 2263–2279, doi:10.1016/S0016-7037(99)00141-6.

Pin, C., P. E. Fonseca, J. L. Paquette, P. Castro, and P. Matte (2008), The ca. 350 Ma Beja igneous complex: A record of transcurrent slab break-off in the Southern Iberia Variscan Belt?, *Tectonophysics*, *461*, 356–377, doi:10.1016/j.tecto.2008.06.001.

Pirajno, F. (2000), *Ore Deposits and Mantle Plumes*, pp. 1–556, Kluwer Acad., London.

Plank, T., and C. H. Langmuir (1993), Tracing trace-elements from sediment input to volcanic output at subduction zones, *Nature*, *362*, 739–743, doi:10.1038/362739a0.

Plank, T., and C. H. Langmuir (1998), The chemical composition of subducting sediment and its consequences for the crust and mantle, *Chem. Geol.*, *145*, 325–394, doi:10.1016/S0009-2541(97)00150-2.

Priestley, K., E. Debayle, D. McKenzie, and S. Pilidou (2006), Upper mantle structure of eastern Asia from multimode surface waveform tomography, *J. Geophys. Res.*, *111*, B10304, doi:10.1029/2005JB004082.

Qian, Q., J. Gao, R. Klemd, G. Q. He, B. Song, D. Y. Liu, and R. H. Xu (2009), Early Paleozoic tectonic evolution of the Chinese South Tianshan Orogen: Constraints from SHRIMP zircon U-Pb geochronology and geochemistry of basaltic and dioritic rocks from Xiate, NW China, *Int. J. Earth Sci.*, *98*, 551–569, doi:10.1007/s00531-007-0268-x.

Qin, K. Z., B. X. Su, P. A. Sakyi, D. M. Tang, X. H. Li, H. Sun, Q. H. Xiao, and P. P. Liu (2011), SIMS zircon U-Pb geochronology and Sr-Nd isotopes of Ni-Cu Bearing mafic-ultramafic intrusions in eastern Tianshan and Beishan in correlation with flood basalts in Tarim basin (NW China): Constraints on a ca. 280 Ma mantle plume, *Am. J. Sci.*, *311*, 237–260, doi:10.2475/03.2011.03.

Rickwood, P. C. (1989), Boundary lines within petrologic diagrams which use oxides of major and minor elements, *Lithos*, *22*, 247–263, doi:10.1016/0024-4937(89)90028-5.

Roberts, N. M. W., T. Slagstad, R. P. Parrish, M. J. Norry, M. Marker, and M. S. A. Horstwood (2013), Sedimentary recycling in arc magmas: Geochemical and U-Pb-Hf-O constraints on the Mesoproterozoic Suldal Arc, SW Norway, *Contrib. Mineral. Petrol.*, *165*, 507–523, doi:10.1007/s00410-012-0820-y.

Rocha, E. R. V., I. S. Puchtel, L. S. Marques, R. J. Walker, F. B. Machado, A. J. R. Nardy, M. Babinski, and A. M. G. Figueiredo (2012), Re-Os isotope and highly siderophile element systematics of the Paraná continental flood basalts (Brazil), *Earth Planet. Sci. Lett.*, *337–338*, 164–173, doi:10.1016/j.epsl.2012.04.050.

Rudnick, R. L., and S. Gao (2003), Composition of the continental crust, in *The Crust Treatise on Geochemistry*, vol. 3, edited by R. L. Rudnick, pp. 1–64, Elsevier, Oxford.

Saleeby, J., M. Ducea, and D. Clemens-Knott (2003), Production and loss of high-density batholithic root, southern Sierra Nevada, California, *Tectonics*, *22*(6), 1064, doi:10.1029/2002TC001374.

Şengör, A. M. C., B. A. Natal'in, and U. S. Burtman (1993), Evolution of the Altaid tectonic collage and Paleozoic crustal growth in Eurasia, *Nature*, *364*, 209–304, doi:10.1038/364299a0.

Sleep, N. H. (1997), Lateral flow and ponding of starting plume material, *J. Geophys. Res.*, *102*, 10,001–10,012, doi:10.1029/97JB00551.

Sleep, N. H., C. J. Ebinger, and J. M. Kendall (2002), Deflection of mantle plume material by cratonic keels, *Early Earth: Phys., Chem. Biol. Dev.*, *199*, 135–150, doi:10.1144/GSL.SP.2002.199.01.08.

Stacey, J. S., and J. D. Kramers (1975), Approximation of terrestrial lead isotope evolution by a two-stage model, *Earth Planet. Sci. Lett.*, *26*, 207–221, doi:10.1016/0012-821X(75)90088-6.

Stefano, C. J., S. B. Mukasa, A. Andronikov, and W. P. Leeman (2011), Water and volatile systematics of olivine-hosted melt inclusions from the Yellowstone hotspot track, *Contrib. Mineral. Petrol.*, *161*, 615–633, doi:10.1007/s00410-010-0553-8.

Sun, L. H., Y. J. Wang, W. M. Fan, and T. P. Peng (2007), Petrogenesis and tectonic significances of the diabase dikes in the Bachu area, Xinjiang [in Chinese with English abstract], *Acta Petrol. Sin.*, *23*, 1369–1380.

Sun, L. H., Y. J. Wang, W. M. Fan, and J. W. Zi (2008), A further discussion of the petrogenesis and tectonic implication of the Mazhashan syenites in the Bachu area [in Chinese with English abstract], *J. Jilin Univ. (Earth Sci. Ed.)*, *38*, 8–20.

Sun, S. S., and W. F. McDonough (1989), Chemical and isotopic systematics of oceanic basalts: Implications for mantle composition and processes, *Geol. Soc. London, Spec. Publ.*, *42*, 313–345.

Tannaka, T., et al. (2000), JNdi-1: A neodymium isotopic reference in consistency with LaJolla neodymium, *Chem. Geol.*, *168*, 279–281, doi:10.1016/S0009-2541(00)00198-4.

Tatsumi, Y. (1986), Formation of the volcanic front in subduction zones, *Geophys. Res. Lett.*, *13*, 717–720, doi:10.1029/GL013i008p00717.

Tian, W., I. H. Campbell, C. M. Allen, P. Guan, W. Q. Pan, M. M. Chen, H. J. Yu, and W. P. Zhu (2010), The Tarim picrite-basalt-rhyolite suite, a Permian flood basalt from northwest China with contrasting rhyolites produced by fractional crystallization and anatexis, *Contrib. Mineral. Petrol.*, *160*, 407–425, doi:10.1007/s00410-009-0485-3.

Tollari, N., S. J. Barnes, R. A. Cox, and H. Nabil (2008), Trace element concentrations in apatites from the Sept-Iles Intrusive Suite, Canada—Implications for the genesis of nelsonites, *Chem. Geol.*, *252*, 180–190, doi:10.1016/j.chemgeo.2008.02.016.

Tu, X. L., H. Zhang, W. F. Deng, M. X. Ling, H. Y. Liang, Y. Liu, and W. D. Sun (2011),. Application of RESOlution *in-situ* laser ablation ICP-MS in trace element analyses [in Chinese with English abstract], *Geochimica*, *40*, 83–89.

Turner, S. P., J. P. Platt, R. M. M. George, S. P. Kelley, D. G. Pearson, and G. M. Nowell (1999), Magmatism associated with orogenic collapse of the Betic-Alboran Domain, SE Spain, *J. Petrol.*, *40*, 1011–1036, doi:10.1093/petrology/40.6.1011.

Väisänen, M., I. Mänttäri, L. M. Kriegsman, and P. Hölttä (2000), Tectonic setting of post-collisional magmatism in the Palaeoproterozoic Svecofennian Orogen, SW Finland, *Lithos*, *54*, 63–81, doi:10.1016/S0024-4937(00)00018-9.

Valley, J. W., P. D. Kinny, D. J. Schulze, and M. J. Spicuzza (1998), Zircon megacrysts from kimberlite: Oxygen isotope variability among mantle melts, *Contrib. Mineral. Petrol.*, *133*, 1–11, doi:10.1007/s004100050432.

Vervoort, J., T. Plank, and J. Prytulak (2011), The Hf-Nd isotopic composition of marine sediments, *Geochim. Cosmochim. Acta*, *75*, 5903–5926, doi:10.1016/j.gca.2011.07.046.

Villemaire, M., F. A. Darbyshire, and I. D. Bastow (2012), P-wave tomography of eastern North America: Evidence for mantle evolution from Archean to Phanerozoic, and modification during subsequent hot spot tectonism, *J. Geophys. Res.*, *117*, B12302, doi:10.1029/2012JB009639.

Wei, G. J., X. R. Liang, X. H. Li, and Y. Liu (2002), Precise measurement of Sr isotopic compositions of liquid and solid base using (LA) MCICP-MS [in Chinese with English abstract], *Geochimica*, *31*, 295–305.

Wei, X., and Y. G. Xu (2011), Petrogenesis of Xiaohaizi syenite complex from Bachu area, Tarim [in Chinese with English abstract], *Acta Petrol. Sin.*, *27*, 2984–3004.

Wei, X., Y. G. Xu, Y. X. Feng, and J. X. Zhao (2014), Plume-lithosphere interaction in the generation of the Tarim large igneous province, NW China: Geochronological and geochemical constraints, *Am. J. Sci.*, *314*, 314–356, doi:10.2475/01.2014.09.

White, R., and D. McKenzie (1989), Magmatism at rift zones: The generation of volcanic continental margins and flood basalts, *J. Geophys. Res.*, *94*, 7685–7729, doi:10.1029/JB094iB06p07685.

Wiedenbeck, M., P. Alle, F. Corfu, W. L. Griffin, M. Meier, F. Oberli, A. Vonquadt, J. C. Roddick, and W. Speigel (1995), Three natural zircon standards for U-Th-Pb, Lu-Hf, trace-element and REE analyses, *Geostand. Newsl.*, *19*, 1–23, doi:10.1111/j.1751-908X.1995.tb00147.x.

Wiedenbeck, M., et al. (2004), Further characterisation of the 91500 zircon crystal, *Geostand. Geoanal. Res.*, *28*, 9–39, doi:10.1111/j.1751-908X.2004.tb01041.x.

Windley, B. F., M. B. Allen, C. Zhang, Z. Y. Zhao, and G. R. Wang (1990), Paleozoic accretion and Cenozoic redeformation of the Chinese Tien-Shan-Range, central-Asia, *Geology*, *18*, 128–131, doi:10.1130/0091-7613(1990)018<0128:PAACRO>2.3.CO;2.

Windley, B. F., D. Alexeiev, W. J. Xiao, A. Kröner, and G. Badarch (2007), Tectonic models for accretion of the Central Asian Orogenic Belt, *J. Geol. Soc.*, *164*, 31–47, doi:10.1144/0016-76492006-022.

Wu, F. Y., Y. H. Yang, L. W. Xie, J. H. Yang, and P. Xu (2006), Hf isotopic compositions of the standard zircons and baddeleyites used in U-Pb geochronology, *Chem. Geol.*, *234*, 105–126, doi:10.1016/j.chemgeo.2006.05.003.

Xiao, W. J., B. F. Windley, B. C. Huang, C. M. Han, C. Yuan, H. L. Chen, M. Sun, S. Sun, and J. L. Li (2009a), End-Permian to mid-Triassic termination of the accretionary processes of the southern Altaids: Implications for the geodynamic evolution, Phanerozoic continental growth, and metallogeny of Central Asia, *Int. J. Earth Sci. (Geol. Rundsch.)*, *98*, 1189–1217, doi:10.1007/s00531-008-0407-z.

Xiao, W. J., B. F. Windley, C. Yuan, M. Sun, C. M. Han, S. F. Lin, H. L. Chen, Q. R. Yan, D. Y. Liu, and K. Z. Qin (2009b), Paleozoic multiple subduction-accretion processes of the southern Altaids, *Am. J. Sci.*, *309*, 221–270, doi:10.2475/03.2009.02.

Xu, X. Y., H. L. Wang, P. Li, J. L. Chen, Z. P. Ma, T. Zhu, N. Wang, and Y. P. Dong (2013), Geochemistry and geochronology of Paleozoic intrusions in the Nalati (Narati) area in Western Tianshan, Xinjiang, China: Implications for Paleozoic tectonic evolution, *J. Asian Earth Sci.*, *72*, 33–62, doi:10.1016/j.jseaes.2012.11.023.

Xu, Y. G., X. Wei, Z. Y. Luo, H. Q. Liu, and J. Cao (2014), The Early Permian Tarim Large Igneous Province: Main characteristics and a plume incubation model, *Lithos*, *204*, 20–35, doi:10.1016/j.lithos.2014.02.015.

Xue, Y. X., and Y. F. Zhu (2009), Zircon SHRIMP chronology and geochemistry of the Haladala gabbro in south-western Tianshan Mountains [in Chinese with English abstract], *Acta Petrol. Sin.*, *25*, 1353–1363.

Yin, A., S. Nie, P. Craig, T. M. Harrison, F. J. Ryerson, X. L. Qian, and G. Yang (1998), Late Cenozoic tectonic evolution of the southern Chinese Tian Shan, *Tectonics*, *17*, 1–27, doi:10.1029/97TC03140.

Yu, J. C., X. X. Mo, X. H. Yu, G. C. Dong, Q. Fu, and F. C. Xing (2012), Geochemical characteristics and petrogenesis of Permian basaltic rocks in Keping area, western Tarim basin: A record of plume-lithosphere interaction, *J. Earth Sci.*, *23*, 442–454, doi:10.1007/s12583-012-0267-0.

Yu, X., S. F. Yang, H. L. Chen, Z. Q. Chen, Z. L. Li, G. E. Batt, and Y. Q. Li (2011), Permian flood basalts from the Tarim Basin, northwest China: SHRIMP zircon U-Pb dating and geochemical characteristics, *Gondwana Res.*, *20*, 485–497, doi:10.1016/j.gr.2010.11.009.

Yuan, F., T. F. Zhou, D. Y. Zhang, S. M. Jowitt, R. R. Keays, S. Liu, and Y. Fan (2012), Siderophile and chalcophile metal variations in basalts: Implications for the sulfide saturation history and Ni-Cu-PGE mineralization potential of the Tarim continental flood basalt province, Xinjiang Province, China, *Ore Geol. Rev.*, *45*, 5–15, doi:10.1016/j.oregeorev.2011.04.003.

Zhang, C. L., Y. G. Xu, Z. X. Li, H. Y. Wang, and H. M. Ye (2010a), Diverse Permian magmatism in the Tarim Block, NW China: Genetically linked to the Permian Tarim mantle plume? *Lithos*, *119*, 537–552, doi:10.1016/j.lithos.2010.08.007.

Zhang, C. L., Z. X. Li, X. H. Li, Y. G. Xu, G. Zhou, and H. M. Ye (2010b), A Permian large igneous province in Tarim and Central Asian orogenic belt, NW China: Results of a ca 275 Ma mantle plume? *Geol. Soc. Am. Bull.*, *122*, 2020–2040, doi:10.1130/B30007.1.

Zhang, D. Y., T. F. Zhou, F. Yuan, S. M. Jowitt, Y. Fan, and S. Liu (2012), Source, evolution and emplacement of Permian Tarim basalts: Evidence from U-Pb dating, Sr–Nd–Pb–Hf isotope systematics and whole rock geochemistry of basalts from the Keping area, Xinjiang Uygur Autonomous region, northwest China, *J. Asian Earth Sci.*, *49*, 175–190, doi:10.1016/j.jseaes.2011.10.018.

Zhang, D. Y., Z. C. Zhang, M. Santosh, Z. G. Cheng, H. Huang, and J. L. Kang (2013), Perovskite and baddeleyite from kimberlitic intrusions in the Tarim large igneous province signal the onset of an end-Carboniferous mantle plume, *Earth Planet. Sci. Lett.*, *361*, 238–248, doi:10.1016/j.epsl.2012.10.034.

Zhang, Y. T., J. Q. Liu, and Z. F. Guo (2010c), Permian basaltic rocks in the Tarim basin, NW China: Implications for plume-lithosphere interaction, *Gondwana Res.*, *18*, 596–610, doi:10.1016/j.gr.2010.03.006.

Zhang, Y. X., X. D. Li, and J. Zhang (2000), Basic pluton and its tectonic setting in Kaladala of west Tianshan Mountains, China [in Chinese English abstract], *Xinjiang Geol.*, *18*, 256–263.

Zhou, M. F., P. T. Robinson, C. M. Lesher, R. R. Keays, C. J. Zhang, and J. Malpas (2005), Geochemistry, petrogenesis and metallogenesis of the Panzhihua gabbroic layered intrusion and associated Fe-Ti-V oxide deposits, Sichuan Province, SW China, *J. Petrol.*, *46*, 2253–2280, doi:10.1093/petrology/egi054.

Zhou, M. F., J. H. Zhao, C. Y. Jiang, J. F. Gao, W. Wang, and S. H. Yang (2009), OIB-like, heterogeneous mantle sources of Permian basaltic magmatism in the western Tarim Basin, NW China: Implications for a possible Permian large igneous province, *Lithos*, *113*, 583–594, doi:10.1016/j.lithos.2009.06.027.

Zhu, Y. F., X. Guo, B. Song, L. F. Zhang, and L. B. Gu (2009), Petrology, Sr-Nd-Hf isotopic geochemistry and zircon chronology of the Late Palaeozoic volcanic rocks in the southwestern Tianshan Mountains, Xinjiang, NW China, *J. Geol. Soc., London*, *166*, 1085–1099, doi:10.1144/0016-76492008-130.

Zhu, Z. M., Z. H. Zhao, X. L. Xiong, and J. W. Han (2010), Petrogeochemistry of late Paleozoic gabbroic rocks from Tekes County in West Tianshan Mountains [in Chinese English abstract], *Acta Petrol. Mineral.*, *29*, 675–690.

Zindler, A., and S. Hart (1986), Chemical geodynamics, *Annu. Rev. Earth Planet. Sci.*, *14*, 493–571, doi:10.1146/annurev.earth.14.1.493.

Zonenshain, L. P., M. I. Kuzmin, and L. M. Natapov (1990), *Geology of the USSR: A Plate Tectonic Synthesis*, Geodyn. Ser., vol. 21, pp. 1–242, AGU, Washington, D. C.